Polymer
Chemistry

ROYAL SOCIETY
OF CHEMISTRY

PAPER

View Article Online
View Journal | View Issue

Cite this: *Polym. Chem.*, 2025, **16**, 4444

Living ROMP of poly(*m*,*p*-phenylenevinylene) and functionalized norbornene-dicarboximides copolymers: guided synthesis toward enhanced optoelectronic and thermal properties with DFT insights

Mohamed E. Abdu, *[a,b] Mohammed F. Radwan, [a,c] Abdulrahman E. Mesbah,[d] Ye J.hao,[a] Abdelrahman Zkria,[e] Mahmoud Z. Basyouni*[a,f] and Andrew M. Spring*[a]

Received 15th August 2025,
Accepted 16th September 2025

DOI: 10.1039/d5py00818b

rsc.li/polymers

A series of functionalized copolymers is synthesized *via* ring-opening metathesis polymerization (ROMP). Dioctyloxy-substituted [2.2]metaparacyclophane-1,9-diene (**DO-mp-CPDE**) (**M1**), was synthesized and fully characterized by IR, ^{1}D-NMR, and ^{2}D-NMR. A novel fully conjugated polymer, poly(*m*,*p*-phenylenevinylene), along with rod–coil copolymers (**P2–P5**) incorporating **DO-*mp*-CPDE** and non-conjugated units Norbornene Dicarboximides (NDI), was synthesized utilizing ROMP with second-generation Grubbs catalyst (G2). Kinetics studies examined using GPC confirmed controlled living polymerization in homopolymer and block designs, evidenced by PDI 1.10–1.17 and a close agreement between experimental and calculated M_n values. In contrast, random copolymers exhibited broader distributions due to ring strain mismatch. Optical measurements revealed tunable band gaps, E_g^{op} 2.53–2.56 eV, and electrochemical gaps, E_g^{elc} 2.01–2.37 eV, with enhanced conjugation in the homopolymer leading to narrower gaps. Morphological investigations using SEM showed distinct self-assembly behaviours influenced by the polymer chain and the micellization protocol, which explains the enhancement in the optical properties of these polymers with E_g^{op} 2.27–2.41 eV. TGA analysis demonstrated high thermal stability across all polymers, with a range of around 368.2–394.6 °C. DFT and TD-DFT calculations confirmed that the effective conjugation length has been gained in all polymers. These findings highlight the versatility of ROMP in creating conjugated polymers with tunable optoelectronic performance and improved thermal stability, making them promising for flexible electronics applications.

1 Introduction

Rod–coil block copolymers have garnered significant interest due to their ability to self-assemble into well-defined nanostructures such as spheres, lamellae, and gyroids.[1–4] These morphologies arise from the inherent phase separation between rigid (conjugated) and flexible polymer segments, governed by factors like molecular weight, segmental interaction, volume fraction, and chemical composition. In selective solvents, these remarkable amphiphilic copolymers have the fascinating ability to form micelles or hollow nanospheres. This unique property opens up exciting possibilities for innovative applications in nanofabrication, optoelectronics, and targeted delivery systems.[5–14] For conjugated polymers in particular, controlling such nanoscale architectures is critical for optimizing charge transport, film uniformity, and overall device performance.[15–18] These requirements underscore the importance of advanced polymerization techniques that facilitate precise control over molecular structure and dispersity.[19–22] Ring-opening metathesis polymerization (ROMP) has emerged as a powerful synthetic method for preparing well-defined conjugated polymers with excellent architectural control.[23–25] The living nature of ROMP, enabled by robust transition metal catalysts such as Grubbs ruthenium carbene complexes, allows

---

[a] *Department of Interdisciplinary Engineering Sciences, Chemistry and Materials Science, Interdisciplinary Graduate School of Engineering Sciences, Kyushu University, 6-1 Kasuga Park, Fukuoka 816-8580, Japan.*
E-mail: mohamedezzat@zu.edu.eg, abdu.mohamed.056@s.kyushu-u.ac.jp, spring@cm.kyushu-u.ac.jp, mahmoud.basiouny@fsc.bu.edu.eg
[b] *Department of Chemistry, Faculty of Science, Zagazig University, Zagazig, 44519, Egypt*
[c] *Department of Chemistry, Faculty of Science, South Valley University, Qena, 83523, Egypt*
[d] *Department of Chemistry, Faculty of Science, Mansoura University, Mansoura, 35516, Egypt*
[e] *Interdisciplinary Graduate School of Engineering Sciences, Kyushu University, Kasuga, Fukuoka 816-8580, Japan*
[f] *Department of Chemistry, Faculty of Science, Benha University, Benha, 13518, Egypt*

for precise control over molecular weight, narrow polydispersity, and programmable sequence of monomer incorporation. ROMP is also tolerant to a wide range of functional groups. It operates under mild conditions, making it well-suited for synthesizing complex copolymer architectures, including rod–coil systems and donor–acceptor conjugated polymers.[23,26–31]

Among conjugated materials, poly(*p*-phenylene vinylene) (PPV) derivatives have stood out due to their strong luminescence and favorable charge transport properties.[32–35] However, practical applications of PPV-based materials have been hindered by challenges such as poor mechanical properties, aggregation-induced quenching, and limited film processability. To overcome these limitations, we explore the synthesis of PPV-based copolymers *via* ROMP while incorporating norbornene dicarboximide (NDI) units into the polymer backbone. This strategy combines the synthetic precision of ROMP with the multifunctional benefits of NDI to generate polymers with improved performance.[36–43] The incorporation of NDI units offers several key advantages. Their rigid, planar structure enhances mechanical strength and thermal stability, addressing brittleness often seen in traditional PPVs. As electron-deficient acceptors, NDI units also promote donor–acceptor interactions with the electron-rich PPV backbone, enabling bandgap tuning and enhancing charge carrier mobility. Furthermore, NDI's presence disrupts excessive π–π stacking, which often leads to aggregation and defects, thereby improving film formation and morphological uniformity—crucial for device performance.[12,44,45]

This study offers an in-depth exploration of the synthesis of a novel dioctyloxy-substituted [2.2]metaparacyclophane-1,9-diene (**DO-*mp*-CPDE**) (**M1**), characterized by IR, ^{1}D-NMR, and ^{2}D-NMR. Additionally, the strategic synthesis of novel conjugated polymers derived from cyclophanedienes, as shown in Scheme 1, and norbornene-based monomers using ROMP was initiated by the G2 generation. Five polymers were synthesized and studied: one homopolymer (**P1**) based on poly(DO-MPPV), and four copolymers (**P2–P5**), comprising both block and random architectures. Temporal kinetic studies using GPC confirmed the living nature of the polymerization. For example, **P1** exhibited a progressive increase in molecular weight over time, with M_n rising and polydispersity index (PDI) decreasing from 1.44 to 1.10. The block copolymers poly(DO-MPPV-*co*-CH-NDI) (**P2**) and poly(DO-MPPV-*co*-AD-NDI) (**P3**) achieved narrow PDIs and strong agreement between experimental and calculated M_n, demonstrating high precision in chain growth. In contrast, random copolymers poly(DO-MPPV-*co*-CH-NDI) (**P4**) and poly(DO-MPPV-*co*-AD-NDI) (**P5**) displayed broader molecular weight distributions and higher M_n values. Optical characterization showed that **P1** had the narrowest bandgap, E_g^{op} at 2.53 eV in solution, 2.44 eV in film. In comparison, copolymers exhibited E_g^{op} values ranging from 2.40 to 2.56 eV depending on structure and medium. Thermal analysis revealed excellent stability across all polymers, and glass transition temperatures (T_g) increased with norbornene content. Furthermore, cyclic voltammetry confirmed E_g^{elc} values from 2.01 to 2.37 eV, aligning with the observed conjugation trends. SEM imaging of thin films revealed distinct morphological differences, with **P1** forming uniform spherical particles, while **P4** and **P5** showed aggregated and porous structures. The optical and electrochemical measurements and the performed DFT and TD-DFT calculations confirmed that the effective conjugation length has been gained in all of the synthesized polymers. In Addition, the DFT calculations revealed that HOMO and LUMO energy values, when compared with the PCBM, point to the possibility of these polymers acting as donors and the PCBM as acceptor in BHJ organic solar cells. These results highlight how ROMP, combined with rational monomer selection and polymerization strategy, enables precise control over polymer structure and properties, offering a robust platform for developing advanced materials in organic electronics, further promising applications in solar energy conversion.

Mohamed E. Abdu

Mohamed Ezzat received his M. Sc. degree in Organic Chemistry (Polymer chemistry) from Zagazig University, Egypt, in 2020, where his research focused on the synthesis of semiconducting polymers via Suzuki coupling for solar cell applications. From 2020 to 2023, he served as an Assistant Lecturer at Zagazig University. He is currently pursuing his Ph.D. degree at Kyushu University, Japan. His doctoral research is dedicated to the design and synthesis of polymers and copolymers, including rod–coil architectures, via ring-opening metathesis polymerization (ROMP), with an emphasis on their optoelectronic applications.

2 Experimental

For clarity and completeness, detailed information regarding the materials, instrumentation used in this study, and the synthesized intermediates has been provided in the SI.

2.1 Synthesis of dioctyloxy-substituted [2.2]metaparacyclophane-1,9-diene (DO-*mp*-CPDE) (M1)

The oxidation product **6** (0.82 g, 0.001151 mol) was placed in a 250 mL three-neck flask. Dimethylformamide (DMF, 100 mL) was added to the flask, and the resulting mixture was stirred at room temperature for 5 minutes to ensure complete dissolution. The reaction mixture was then heated to 155 °C under a nitrogen atmosphere and maintained at this temperature for 20 hours to facilitate the reaction. After completion, the mixture was allowed to cool to room temperature. The product was then washed with dilute aqueous hydrochloric acid and extracted into chloroform. The organic layer was col-

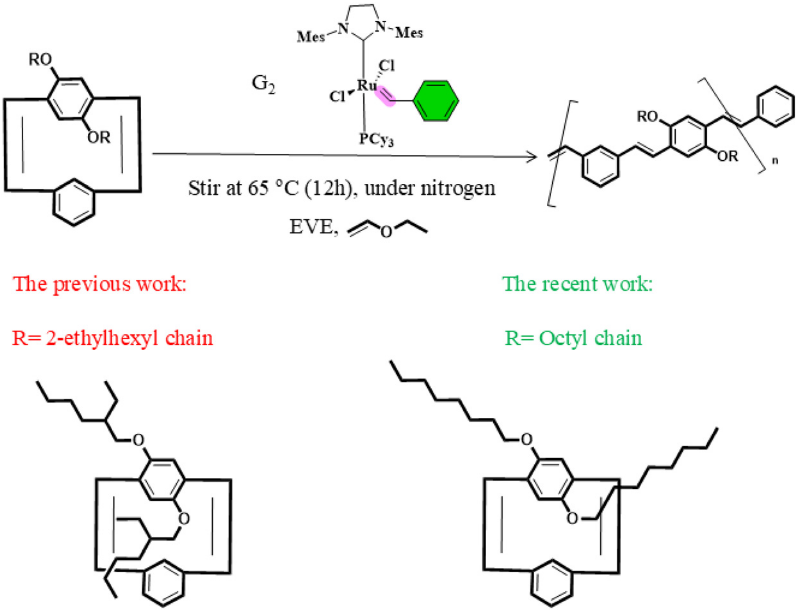

Scheme 1 Illustration of the progression from previous work to the current study using **DO-*mp*-CPDE** (**M1**).

lected, dried over anhydrous sodium sulfate, and concentrated to yield a yellow oil. The crude product was further purified by column chromatography using a solvent system of 20% dichloromethane (DCM) and 80% hexane, yielding the pure product as a clear oil (0.4 g, 75.5%). EI-MS calculated for $C_{32}H_{44}O_2$ *m*/*z*: 460.33; found: *m*/*z* 460.00. IR (KBr, *ν*, cm^{-1}): 3003 ($CH_{aromatic}$), 2920 ($CH_{aliphatic}$), 1467(C=C), 1203 (C–O). ^{1}H NMR (400 MHz, chloroform-D) *δ* 6.96–7.02 (m, 3H), 6.80 (d, *J* = 7.8 Hz, 2H), 6.61 (d, *J* = 10.5 Hz, 2H), 6.13 (s, 2H), 4.83 (s, 1H), 3.73 (q, *J* = 7.2 Hz, 2H), 3.27 (q, *J* = 7.3 Hz, 2H), 1.59 (t, *J* = 6.6 Hz, 4H), 1.27 (s, 20H), 0.88 (t, *J* = 6.2 Hz, 6H) ppm.^{13}C NMR (101 MHz, chloroform-D) *δ* 157.57, 137.23, 135.09, 131.45, 130.85, 130.45, 125.82, 15.32, 117.76, 69.46, 31.94, 29.50, 29.47, 29.36, 26.11, 22.78, 14.24 ppm.

2.2 Synthesis of *N*-cyclo hexyl-(*exo*-norbornene)-5,6-dicarboximide (CH-NDI) 9 (M2)

A solution of *exo*-NDA **8** (10 g, 0.06 mol) and cyclohexyl amine (8.9 g, 0.09 mol) in dry toluene (100 mL) was subjected to reflux for 4 hours, with the reaction progress meticulously monitored *via* TLC until complete consumption of *exo*-NDA was confirmed. Subsequently, the solvent was removed under reduced pressure, yielding an off-white precipitate. This precipitate was dissolved in a biphasic mixture of deionized water and chloroform. The desired product was then isolated by extracting the organic layer, which was subsequently dried over anhydrous sodium sulfate. The solvent was evaporated, and the resultant material was collected and dried, producing a white crystalline solid (14 g, 96%). EI-MS calculated for $C_{14}H_{19}NO_2$ *m*/*z*: 245.14; found: *m*/*z* 245.00. IR (KBr, *ν*, cm^{-1}): 2933 ($CH_{aliphatic}$), 1698 (C=O), 1368 (C–N).^{1}H NMR (400 MHz, chloroform-D) *δ* 6.25 (d, *J* = 1.8 Hz, 2H), 3.87–3.95 (m, 1H), 3.23 (d, *J* = 1.4 Hz, 2H), 2.58 (d, *J* = 1 Hz, 2H), 2.12 (dd, *J* = 22.0, 12.3 Hz, 2H), 1.79 (d, *J* = 13.3 Hz, 2H), 1.45–1.65 (m, 4H), 1.14–1.32 (m, 4H) ppm.^{13}C NMR (101 MHz, chloroform-D) *δ* 178.52, 138.01, 51.91, 47.69, 45.72, 42.90, 28.98, 26.17, 25.32 ppm.

2.3 Synthesis of *N*-adamantyl-(*exo*-norbornene)-5,6-dicarboximide (AD-NDI) 10 (M3)

Following the same procedure employed for synthesizing the **M2**, *exo*-NDA **8** (10 g, 0.06 mol) and adamantly amine (13.6 g, 0.09 mol) in dry toluene (100 mL) under reflux for 4 hours. The desired product was then isolated by extracting the organic layer, which was subsequently dried over anhydrous sodium sulfate. The solvent was evaporated, and the resultant material was collected and dried, producing a white crystalline solid (13 g, 96%). EI-MS calculated for $C_{19}H_{23}NO_2$ *m*/*z*: 297.17; found: *m*/*z* 297.00 IR (KBr, *ν*, cm^{-1}): 2983 ($CH_{aliphatic}$), 1699 (C=O), 1334 (C–N).^{1}H NMR (400 MHz, chloroform-D) *δ* 6.23 (s, 2H), 3.20 (s, 2H), 2.46 (s, 2H), 2.38 (s, 6H), 2.09 (s, 3H), 1.66–1.73 (m, 6H), 1.43 (d, *J* = 11.0 Hz, 1H), 1.29 (d, *J* = 9.6 Hz, 1H) ppm.^{13}C NMR (101 MHz, chloroform-D) *δ* 179.83, 137.97, 61.65, 47.43, 45.97, 42.57, 39.36, 36.25, 29.83 ppm.

2.4 Synthesis of homopolymer poly(DO-MPPV) P1

The target monomer **M1** (92.14 mg, 0.2 mmol) was transferred into a carousel tube under a carefully maintained nitrogen atmosphere and dissolved in 0.5 mL of anhydrous dichloroethane (DCE). The reaction temperature was gradually increased to 65 °C under a reflux system. Simultaneously, a solution of the G2 generation (4.40 mg) was prepared in 0.2 mL of anhydrous DCE. Using a syringe, the initiator solution was swiftly injected into the reaction flask, and the mixture was maintained under these conditions for 8 hours. The progress of the reaction was closely monitored using TLC until the complete consumption of **M1** was confirmed. Subsequently, the temperature of the reaction tube was slowly reduced to room temperature (RT), and the end-capping process was initiated by rapidly adding ethyl vinyl ether (EVE, 2 mL) to the reaction tube, followed by stirring for an additional 2 hours. The resulting mixture was concentrated under reduced pressure and precipitated in methanol, and the crude polymer was filtered using a silica Giga tube. Purification was achieved through repeated washing with methanol. The final polymeric product, **P1**, was obtained as a dark yellow precipitate with a yield of 75 mg (81%). IR (KBr, ν, cm^{-1}): 3020 ($CH_{aromatic}$), 2906 ($CH_{aliphatic}$), 1593(C=C), 1195 (C–O).^{1}H-NMR (400 MHz, $CDCl_3$) δ 7.53–7.28 (br-m, 3H), 7.24–7.20 (br-m, 3H), 7.15–7.03 (br-m, 2H), 6.92–6.45 (br-m, 2H), 4.01 (br-t, *J* = 14.6 Hz, 2H), 3.53 (br-t, *J* = 5.9 Hz, 2H), 1.91–1.09 (br-m, 24H), 0.92–0.77 (br-m, 6H).

2.5 Synthesis of block copolymer poly(DO-MPPV-*co*-CH-NDI) P2

Following a procedure analogous to that employed for the synthesis of **P1**, the polymerization of 0.5 ml of the solution **DO-*mp*-CPDE** (92.14 mg, 0.2 mmol) was carried out. A solution of the G2 generation (4.40 mg) was prepared in 0.2 mL of DCE. After 8 hours, the complete consumption of monomers was confirmed by monitoring the reaction progress using TLC. Subsequently, the reaction temperature was gradually reduced to 30 °C. Under ambient conditions, a solution of **M2** (49.06 mg, 0.2 mmol) was swiftly introduced into the reaction tube and allowed to react for an additional 2 hours. The end-capping process was initiated by rapidly adding EVE (2 mL) to the reaction tube and stirring for 2 hours. The resulting mixture was concentrated under reduced pressure and precipitated in methanol, and the crude polymer was filtered using a silica Giga tube. Purification was achieved through repeated washing with methanol. The final polymeric product, **P2**, was obtained as a yellowish-green precipitate with a yield of 123 mg (87%). IR (KBr, ν, cm^{-1}): 3019 ($CH_{aromatic}$), 2924 ($CH_{aliphatic}$), 1700 (C=O), 1355 (C–N). ^{1}H-NMR (400 MHz, $CDCl_3$) δ 7.32–7.48 (br-m, 3H), 7.15–7.18 (br-m, 3H), 7.03–7.11 (br-m, 2H), 6.45–6.92 (br-m, 2H), 5.72 (br-d, *J* = 9.1 Hz, 1H), 5.46 (br-d, *J* = 15.6 Hz, 1H), 3.82–4.00 (br-m, 3H), 3.52 (br-t, *J* = 5.3 Hz, 2H), 2.61–3.25 (br-m, 4H), 1.18–2.17 (br-m, 34H), 0.92–0.85 (br-t, *J* = 5.5 Hz, 6H) Fig. S11a.

2.6 Synthesis of block copolymer poly(DO-MPPV-*co*-AD-NDI) P3

In a similar protocol for synthesizing **P2**, the cyclophane product **DO-*mp*-CPDE** (92.14 mg, 0.2 mmol) was dissolved in 0.5 mL of anhydrous DCE. The reaction mixture was gradually heated to 65 °C under reflux conditions, after which a solution of the G2 generation initiator (4.40 mg) in 0.2 mL of anhydrous DCE was introduced. The temperature was then progressively lowered to 30 °C. Under ambient conditions, a solution of **M3** (59.48 mg, 0.2 mmol) was swiftly added to the reaction vessel. The polymerization process successfully yielded the final polymeric product, **P3**, which precipitated as a yellowish-green solid with an isolated yield of 137 mg (90%), indicating an efficient synthetic approach. IR (KBr, ν, cm^{-1}): 3055 ($CH_{aromatic}$), 2925 ($CH_{aliphatic}$), 1692 (C=O), 1331 (C–N). ^{1}H-NMR (400 MHz, $CDCl_3$) δ 7.29–7.47 (br-m, 3H), 7.14 (br-d, *J* = 12.8 Hz, 3H), 7.01–7.08 (br-m, 2H), 6.41–6.89 (br-m, 2H), 5.66 (br-s, 1H), 5.41 (br-s, 1H), 3.97 (br-d, *J* = 33.4 Hz, 2H), 3.49 (br-d, *J* = 11.4 Hz, 2H), 2.58–3.23 (br-m, 4H), 2.33 (br-s, 6H), 2.04 (br-s, 7H), 1.17–1.81 (br-m, 32H), 0.81 (br-t, *J* = 6.4 Hz, 6H) Fig. S11b.

2.7 Synthesis of random copolymer poly(DO-MPPV-*co*-CH-NDI) P4

Under an inert nitrogen atmosphere, equimolar quantities of compound **DO-*mp*-CPDE** (92.14 mg, 0.2 mmol) and compound **M2** (49.06 mg, 0.2 mmol) were introduced into a carousel tube and dissolved in 0.5 mL of anhydrous DCE. The reaction mixture was then gradually heated to 65 °C under reflux conditions. Simultaneously, a solution of the G2 generation (4.4 mg) was prepared in 0.2 mL of anhydrous DCE and promptly injected into the reaction vessel using a syringe. The progression of the polymerization was monitored *via* TLC until the complete consumption of **M1** and **M2** was confirmed. Following this, the reaction temperature was gradually reduced to RT. The end-capping step was initiated by rapidly introducing an excess of EVE (2 mL) into the reaction mixture, which was subsequently stirred for an additional 2 hours. The polymeric solution was then concentrated under reduced pressure and precipitated in methanol. The crude polymer was isolated by filtration through a silica Giga tube and further purified through successive washing with methanol. The final polymeric product, **P4**, was obtained as a yellowish-green precipitate with a remarkably high yield of 100 mg (71%). IR (KBr, ν, cm^{-1}): 3023 ($CH_{aromatic}$), 2916 ($CH_{aliphatic}$), 1697 (C=O), 1367 (C–N). ^{1}H-NMR (400 MHz, $CDCl_3$) δ 7.34–7.65 (br-m, 3H), 7.17 (br-d, *J* = 14.2 Hz, 3H), 7.04–7.10 (br-m, 2H), 6.46–6.92 (br-m, 2H), 5.73 (br-s, 1H), 5.47 (br-d, *J* = 16.0 Hz, 1H), 3.87–4.11 (br-m, 3H), 3.52 (br-s, 2H), 2.61–3.25 (br-m, 4H), 1.18–2.12 (br-m, 34H), 0.85 (br-d, *J* = 5.9 Hz, 6H) Fig. S12a.

2.8 Synthesis of random copolymer poly(DO-MPPV-*co*-AD-NDI) P5

Following an identical procedure to that employed for the synthesis of **P4**, monomer **DO-*mp*-CPDE** (92.14 mg, 0.2 mmol) and compound **M2** (59.48 mg, 0.2 mmol) were added to a carousel tube and dissolved in 0.5 mL of anhydrous DCE. The G2 generation (4.40 mg) was introduced, and the reaction temperature was gradually raised to 65 °C under a reflux system. The final polymeric product, **P5**, was obtained as a yellowish-green precipitate with a yield of 125 mg (82%). IR (KBr, ν, cm^{-1}): 3054 ($CH_{aromatic}$), 2915 ($CH_{aliphatic}$), 1694 (C=O), 1340 (C–N). ^{1}H-NMR (400 MHz, $CDCl_3$) δ 7.29–7.51 (br-m, 3H), 7.13–7.21 (br-m, 3H), 7.03–7.10 (br-m, 2H), 6.45–6.91 (br-m, 2H), 5.69 (br-s, 1H), 5.42 (br-s, 1H), 4.01 (br-d, *J* = 31.6 Hz, 2H), 3.52 (br-t, *J* = 6.2 Hz, 2H), 2.59–3.20 (br-m, 4H), 2.37 (br-s, 8H), 2.08 (br-s, 5H), 1.18–1.84 (br-m, 32H), 0.82–0.86 (br-m, 6H) Fig. S12b.

3 Results and discussion

3.1 Monomers synthesis and characterization

The 1st monomer, **DO-*mp*-CPDE**, was synthesized *via* modified thermal elimination (**pyrolysis**) for oxidation products **6** at 155 °C in DMF in a good yield of 75.5%,[13,46] where the compound **6** is a synthesized intermediate obtained from the multi-step route depicted in Scheme 2. The detailed synthesis and characterization of intermediate **6** are provided in the SI. In Scheme 3, the 2nd and 3rd monomers were obtained through a multistep reaction sequence, including a Diels-Alder reaction to yield a mixture of *endo* and *exo*-NDA, which undergoes recrystallization three times in chlorobenzene to afford the pure *exo*-NDA **8**,[47–49] which acts as an anhydride. Also, the *exo* form of norbornene dicarboxy anhydride was used for polymerization due to being more thermodynamically favored and very reactive with the Grubbs catalyst for ROMP, while the *endo* form was not considered.[50] This anhydride subsequently undergoes imidization upon reaction with a primary amine, such as cyclohexylamine or adamantylamine, forming **M2** and **M3** in a high yield of 96% for both. On the other hand, all intermediates were synthesized and thoroughly characterized, with detailed information provided in the SI.

The spectroscopic analysis of **M1** strongly aligns with the proposed molecular structure, as confirmed by FTIR data presented in Fig. S11. Additionally, the ^{1}H-NMR spectrum exhibits key diagnostic signals. A multiplet at δ 6.96–7.02 ppm corresponds to the substituted phenyl ring's aromatic protons (H-a). Two distinct doublets at δ 6.80 and 6.61 ppm, attributed to the vinylic protons (H-**b** and H-**c**), exhibit coupling constants of J = 7.8 Hz and J = 10.5 Hz, respectively. Furthermore, two singlet peaks appear at δ 6.13 and 4.83 ppm, corresponding to the two

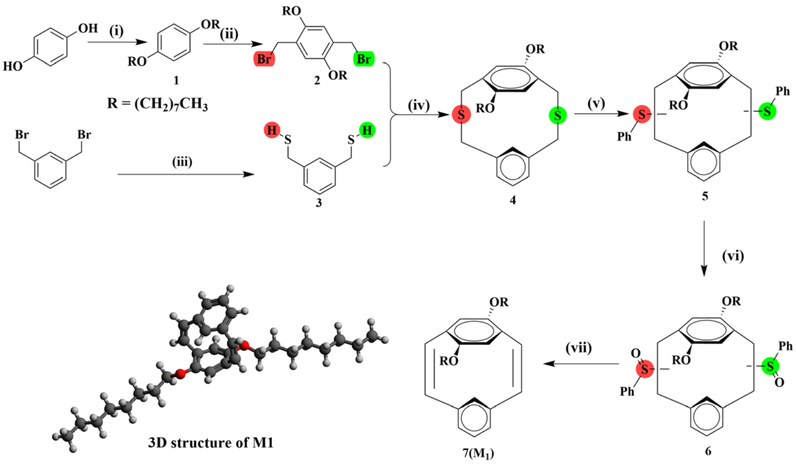

Scheme 2 Synthesis and 3D structure of **DO-*mp*-CPDE** (**M1**). (i) 1-Bromooctane, K_2CO_3, acetonitrile, 80 °C, 48 h, (ii) paraformaldehyde, HBr, acetic acid, 70 °C, 6 h, (iii) a-thiourea, ethanol, 90 °C, 5 h; b-$KOH_{(aq.)}$, 110 °C, 2 h; c-H_2SO_4, RT, 1 h, (iv) $KOH_{(alc.)}$, benzene, RT, 72 h, (v) anthranilic acid, isoamyl nitrite, dry DCE, 85 °C, 1 h, (vi) H_2O_2, acetic acid, RT, 8 h, and (vii) DMF, 150 °C, 20 h.

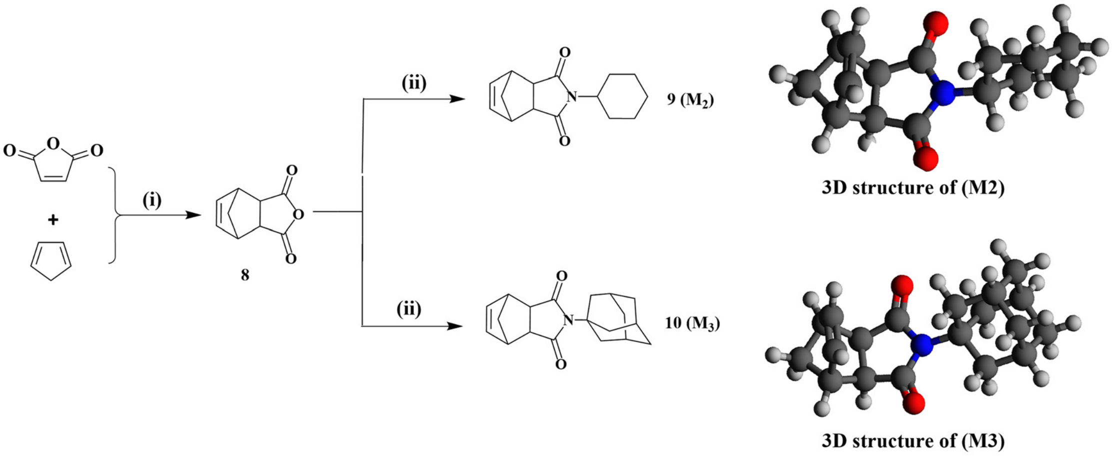

Scheme 3 Synthesis and 3D structure of NDI-monomers (**M2**, **M3**). (i) *o*-Dichlorobenzene, 200 °C, 1.5 h, (ii) recrystallization/chlorobenzene, (iii) dry toluene, reflux, 4 h.

protons (H-**d**) of the substituted phenyl ring and the single proton (H-**e**) of the unsubstituted phenyl ring in sequence. Regarding the alkyl chain, the α-methylene group adjacent to the oxygen atom ($-\mathrm{OCH_2}-$) presents two distinct quartet peaks at δ 3.73 and 3.27 ppm, with coupling constants of J = 7.2 Hz and J = 7.3 Hz, respectively. A triplet at δ 1.59 ppm corresponds to (H-**2**), while a singlet at δ 1.27 ppm is assigned to (H-**3**) with J = 6.6 Hz. The terminal methyl group exhibits a characteristic triplet at δ 0.88 ppm with a coupling constant of J = 6.2 Hz, further confirming the expected structural integrity of **M1** Fig. 1b. The ^{2}D-NMR, including HMQC to confirm proton–carbon correlations, is provided in Fig. S7, and the COSY spectrum exhibits strong correlations between the protons of the unsubstituted aromatic ring (H-**a**) and the vinylic proton (H-**b**), affirming the presence of the expected conjugated system.

Additionally, the well-defined correlation between the α-methylene group ($-\mathrm{OCH_2}-$) and the adjacent methylene proton (H-**2**) unequivocally confirms the successful etherification process. Furthermore, the continuous correlation observed between the subsequent methylene groups (H-**3**) and the terminal methyl group (H-**4**) substantiates the linear connectivity along the entire length of the octyloxy chain, as depicted in Fig. 1c.

The ^{13}C-NMR spectrum provides definitive structural validation, presenting well-resolved signals across both the aromatic and aliphatic regions. The characteristic sp^2-hybridized carbon atoms appear within the range of δ 117.76–157.57 ppm, with the most deshielded peak corresponding to the oxygen-substituted aromatic carbon (C-**1**). Additionally, the vinylic carbons (C-**e** and C-**f**) resonate at δ 130.85 and 130.40 ppm, respectively, indicating their conjugated electronic environment. In the sp^3-hybridized region, the α-methylene carbon ($-\mathrm{OCH_2}-$) exhibits a distinct peak at δ 69.46 ppm, confirming its attachment to an electronegative oxygen. The remaining methylene ($-\mathrm{CH_2}-$) groups appear within the expected aliphatic region, while the terminal methyl ($-\mathrm{CH_3}$) carbon is observed at δ 14.24 ppm, reinforcing the presence of a linear alkyl substituent Fig. 1d. The DEPT-135 spectrum distinctly identifies the expected carbon environments in **M1**. The signals corresponding to the aromatic methine (C-**c**, C-**g**, and C-**i**), vinylic methine (C-**e** and C-**f**), and the terminal methyl ($-\mathrm{CH_3}$) group appear upright (positive, +ve), while the quaternary aromatic carbon atoms (C-**a**, C-**b**, and C-**d**) are absent, as expected. Additionally, all methylene ($-\mathrm{CH_2}$) groups (C-**1** to C-**5**) along the extended octyl chain appear inverted (negative, −ve) as shown in Fig. 1e, further validating the anticipated structural framework. These findings strongly support the expected molecular structure of **M1**.

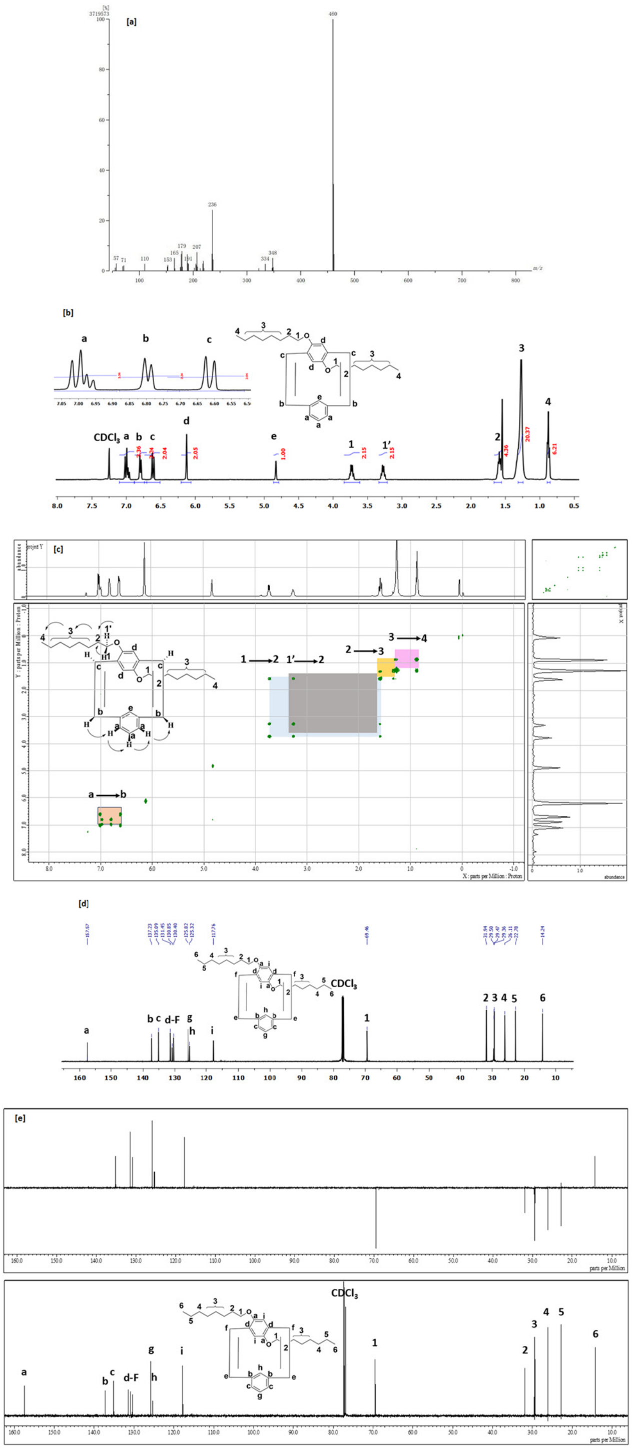

Fig. 1 Spectra of (a) EI-MS, (b) ^{1}H NMR, (c) ^{2}D-NMR COSY, (d) ^{13}C NMR, (e) DEPT for compound **7** (**M1**).

Moreover, the FTIR data are presented in Fig. S12. Confirm that the spectroscopic analysis of CH-NDI (**M2**) strongly agrees with the proposed molecular structure. Additionally, the ^{1}H-NMR spectrum provides essential diagnostic peaks, as illustrated in Fig. 2b, which displays key signals corresponding to vinylic hydrogen. Notably, the vinylic proton (H-**1**) is a doublet with a significant downfield shift at δ 6.25 ppm, attributed to the cycloalkene system's high ring strain, with a J = 1.8 Hz coupling constant. Furthermore, the methine proton (H-**2**), which is directly bonded to the nitrogen atom, is observed as a multiplet with a lower chemical shift, ranging from δ 3.87–3.95 ppm. In addition, two doublet signals at δ 3.23 ppm and δ 2.58 ppm correspond to (H-**3**) and (H-**4**), with a coupling constant of J = 1.41 and 1 Hz, respectively. Lastly, the remain-

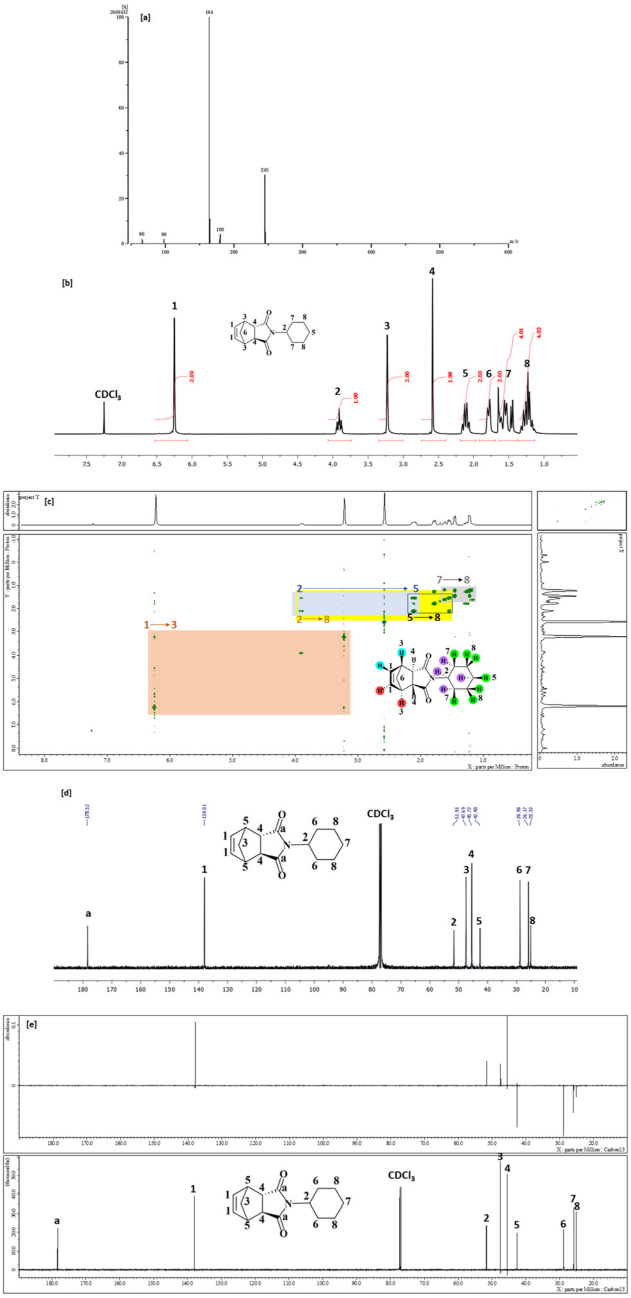

Fig. 2 Spectra of (a) EI-MS, (b) ^{1}H NMR, (c) ^{2}D-NMR COSY, (d) ^{13}C NMR, (e) DEPT for CH-NDI (**M2**).

ing methylene protons appear within the δ 2.12–1.32 ppm range.

The ^{2}D-NMR COSY spectrum also exhibits strong correlations between the vinylic proton (H-1) and the methine proton (H-3), confirming the anticipated *exo*-isomer. Additionally, there is a well-defined correlation between the methine proton directly adjacent to the nitrogen atom of the imide group (H-2) and the methylene protons (H-7). Furthermore, the continuous correlation observed among the successive methylene groups within the cyclohexyl system is illustrated in Fig. 2c. Additionally, the HMQC to confirm proton–carbon correlations is provided in Fig. S9.

The ^{13}C-NMR spectrum offers clear structural confirmation, displaying distinct signals for sp^2 and sp^3 hybridized carbon atoms. The characteristic sp^2-hybridized carbon atoms are observed at δ 178.52–138.01 ppm, corresponding to the carbonyl group (C-a) and the vinylic group (C-1), respectively. The most deshielded peak, attributed to the methine sp^3 carbon atom (C-2) directly adjacent to the amide nitrogen atom, appears at 51.91 ppm. Additionally, the lower chemical shift values for the sp^3 carbon atoms of the cyclic alkene (C-3 to C-5) are observed in the range of δ 47.69–42.90 ppm. Furthermore, the sp^3 carbon atoms of the methylene groups on the cyclohexyl ring (C-6 to C-8) resonate in the range of δ 28.98–25.32 ppm, as illustrated in Fig. 2d.

The DEPT-135 spectrum further corroborates the anticipated carbon environments in **M2**, as depicted in Fig. 2e. The essential peaks corresponding to the methine carbon atoms (C-1, C-2, C-4, and C-5) exhibit positive (+ve) signals, while the methylene groups display inverted (−ve) signals. Notably, the quaternary carbon atom of the carbonyl group is absent in the DEPT-135 spectrum. Collectively, these results provide robust evidence supporting the predicted molecular structure of **M2**.

Furthermore, the FTIR spectroscopic data, as depicted in Fig. S13, confirm that the AD-NDI (**M3**) analysis aligns closely with the proposed molecular structure. Also, the ^{1}H-NMR spectrum, presented in Fig. 3b, reveals essential diagnostic peaks, including distinct signals associated with vinylic hydrogen atoms. Specifically, the vinylic proton (H-1) is observed as a strong singlet at a significantly downfield chemical shift of δ 6.23 ppm due to the substantial ring strain within the cycloalkene system. Additionally, cycloalkene's methine protons (H-2) and (H-3) appear as a firm singlet at a relatively chemical shift, spanning δ 3.20 and 2.46 ppm, respectively. The two singlet peaks are identified at δ 2.38 and 2.09 ppm, corresponding to protons (H-4 and H-5). The remaining methylene protons (H-6) and (H-7) are observed in the final region of the spectrum, appearing within the chemical shift range of δ 1.66–1.29 ppm. Furthermore, the presence of the expected *exo*-isomer is conclusively verified by the ^{2}D-NMR COSY spectrum, which exhibits significant correlations between the vinylic proton (H-1) and the methine proton (H-2). Notably, the structural integrity of the compound is reinforced by the continuous correlation among the successive methylene groups and methine groups within the adamantyl system (H-4, H-5, and H-6), as illustrated in Fig. 3c. The ^{2}D-NMR, including HMQC, is presented in Fig. S10; these findings provide strong support for the proposed molecular framework.

Additionally, the ^{13}C-NMR spectrum provides definitive structural validation, exhibiting distinct signals corresponding to both sp^2- and sp^3-hybridized carbon atoms. The characteristic sp^2-hybridized carbons resonate within the δ 179.83–137.97 ppm range, corresponding to the carbonyl carbon (C-a) and the vinylic carbon (C-1), respectively. The most deshielded sp^3-hybridized methine carbon (C-2), located adjacent to the amide nitrogen, was observed at 61.56 ppm.

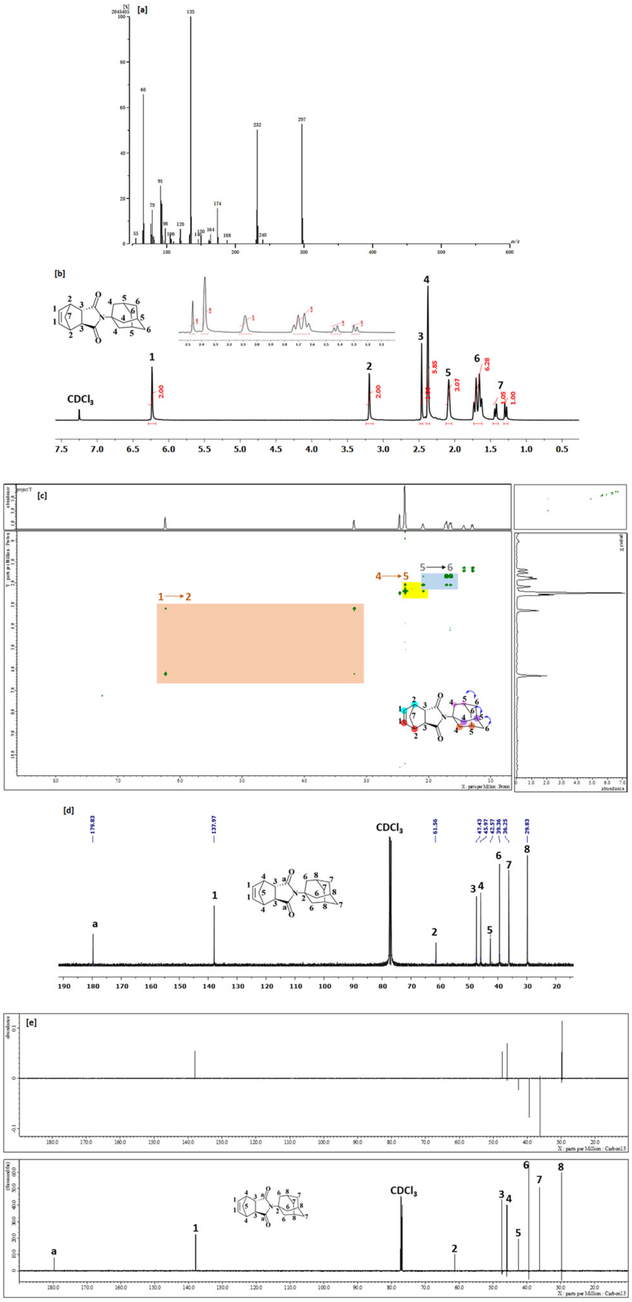

Fig. 3 Spectra of (a) EI-MS, (b) ^{1}H NMR, (c) ^{2}D-NMR COSY, (d) ^{13}C NMR, (e) DEPT for AD-NDI (**M3**).

Furthermore, the sp^3-hybridized carbons within the cyclic alkene system (C-3 to C-5) exhibit lower chemical shifts, ranging from δ 47.43 to 42.57 ppm. The remaining sp^3-hybridized methylene and methine carbons (C-6 to C-8) within the adamantyl ring resonate between δ 39.36–29.83 ppm, as depicted in Fig. 3d. Furthermore, the DEPT-135 spectrum provides an unambiguous characterization of the expected carbon environments in **M3**, as described in Fig. 3e. The methine carbon atoms (C-1, C-3, C-4, and C-8) exhibit distinct positive signals (+ve), whereas the methylene carbon atoms produce inverted (−ve) peaks. Notably, the quaternary carbon atoms associated with the carbonyl groups (C-a and C-2) are absent from the spectrum. These results offer compelling evidence that supports the proposed molecular structure of **M3**.

3.2 Polymers synthesis *via* living ROMP and photoisomerization

The objective of this study is to synthesize the homopolymer derived from the polymerization of the dioctyloxy-substituted [2.2]metaparacyclophane-1,9-diene (**DO-*mp*-CPDE**) (**M1**), along with a series of copolymers incorporating cyclophanediene (**M1**) and norbornene-based monomers, namely CH-NDI (**M2**) and AD-NDI (**M3**), in both random and block macromolecular structures, Scheme 4. Regarding 1,3-phenylenevinylene as a homopolymer, it was synthesized *via* ROMP of the **DO-*mp*-CPDE**, the stoichiometric polymerization process using the initiator of G2 catalyst in the presence of DCE as a solvent at 65 °C. The polymerization process was monitored by TLC, indicating complete conversion within 8 hours. This result suggests a relatively accelerated polymerization rate compared to previous reports.[46] The mixture was initially cooled to room temperature to terminate the reaction, followed by the introduction of ethyl vinyl ether (EVE). The reaction was then stirred continuously for two hours before evaporating the solvent under reduced pressure. For polymer purification, crudes were selectively dissolved in a minimal chloroform volume and precipitated using methanol. This purification process was repeated multiple times to enhance purity. Finally, the resulting polymer underwent extensive washing with methanol to ensure the complete elimination of residual catalyst and drying for 12 hours.

The regio-chemistry of the ring-opening reaction of monomer **M1** was investigated by performing the reaction using a precisely equivalent amount of the catalyst in homo and copolymers. To verify the occurrence of ring opening, the resulting product is anticipated to incorporate two vinylene linkages in both *cis* and *trans* configurations. One linkage is covalently bound to an unsubstituted phenylene ring. In contrast, the other is anchored to a phenylene ring substituted with octyloxy groups and coordinated to a ruthenium carbene center, as shown in Fig. 4.

The spectroscopic analysis of **P1** was confirmed by FTIR data presented in Fig. S11. Additionally, ^{1}H NMR spectroscopy of the **M1** identified two highly shifted peaks. The hydrogen ratio in the end vinylene group attached to the phenylene ring bearing alkoxy substituents relative to that in the end vinylene group bonded to an unsubstituted phenylene ring was determined to be 1 : 0.9, indicating an absence of regioselectivity during polymerization *via* ROMP. Conversely, polymerization of **M2** and **M3** demonstrated high regioselectivity, as evidenced by the presence of a single sharp vinylene resonance at δ 6.25 and 6.23 ppm, respectively (Fig. 2 and 3), with no trace (no detectable signals) of alternative regioisomers observed, and this assignment was further corroborated by HMQC data (Fig. S9 and S10), thereby confirming the high selectivity of the polymerization.[14,48]

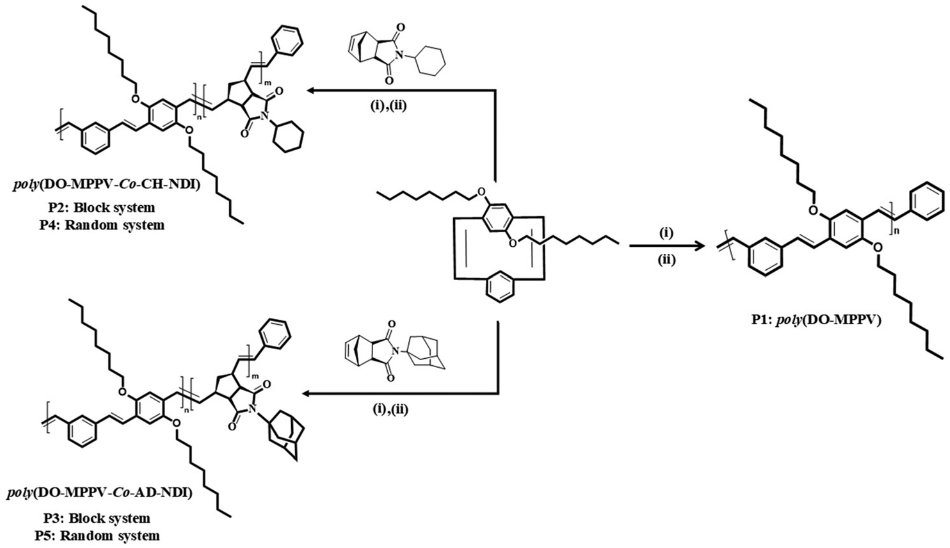

Scheme 4 Synthesis of homo and copolymers (**P1–P5**). (i) G2 generation initiator in DCE at 65 °C (ii) EVE acts as a quencher.

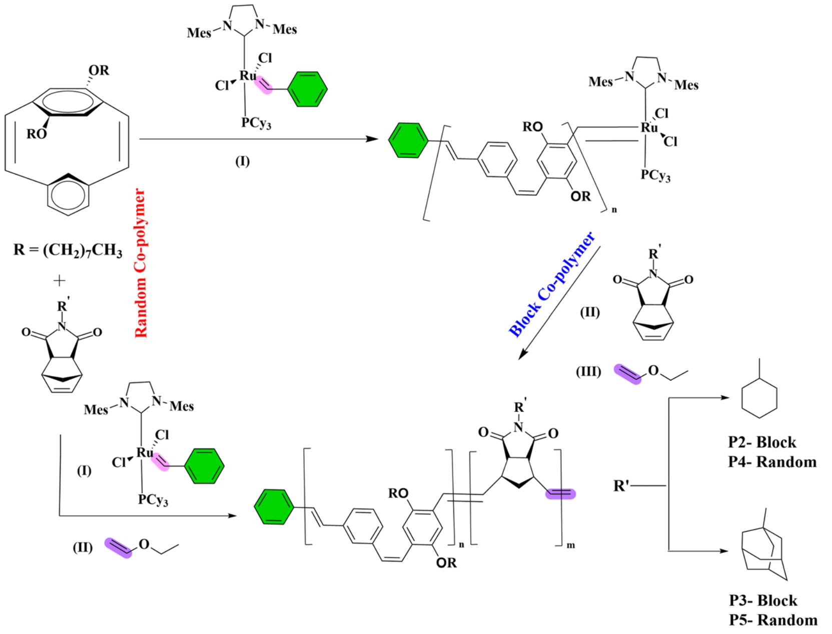

Fig. 4 Reaction mechanism of the synthesized rod–coil design polymers.

Furthermore, the ^{1}H-NMR spectrum of **P1** reveals that the resulting microstructure contains regular alternating *cis* and *trans* configurations in the polymer backbones formed, as evidenced by diagnostic broad signals in Fig. 5b. Quantifying the *cis*-to-*trans* ratio presents a significant challenge due to signal overlap between vinylene group hydrogens and aromatic ring protons. Nevertheless, distinct peaks within the chemical shift at 6.46 to 6.92 ppm range clearly indicate the presence of *cis* vinylene ($-\underline{CH}=\underline{CH}-$). Peaks above δ 7.03 ppm up to 7.15 ppm are attributed to *trans* vinylene, which overlaps with the *ortho* position relative to the hydrogen of phenylene rings and the remaining hydrogen signals of aromatic rings presented above δ 7.25 ppm up to δ 7.50. Regarding the alkyl chain, the α-methylene group adjacent to the oxygen atom ($-O\underline{CH_2}-$) presents two distinct peaks at δ 4.00 and 3.53 ppm; analyzing the values of these prominent key signals reveals a notable downfield shift compared to precursor **M1**.

A stereochemistry of the resulting polymer, **P1**, was performed using ^{1}H-NMR spectroscopy after photoisomerization under UV irradiation at 365 nm for 48 hours, as shown in Fig. 5c. A significant structural transformation was observed, indicated by the downfield shift of the *cis*-configuration signal

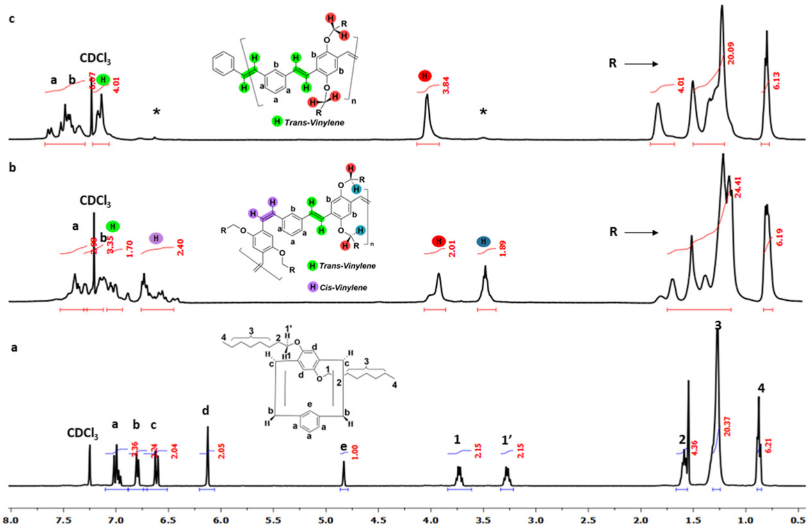

Fig. 5 Spectra of ^{1}H NMR for (a) **DO-*mp*-CPDE**, (b) *cis*/*trans*-poly(DO-MPPV) **P1**, (c) *trans*-poly(DO-MPPV) **P1**.

between the phenylene rings from δ 6.46–6.92 ppm to δ 7.16–7.20 ppm. This shift signifies a transition from the *cis* to the *trans* configuration. Additionally, the peak corresponding to the proton of a methylene group (–O–$\underline{CH}_2$) initially located at 3.53 ppm showed deshielding, shifting to δ 4.01 ppm. These findings collectively confirm that the polymer has predominantly adopted the *trans* configuration, which is inherently more stable.

Additionally, to synthesize the block design (ideal rod–coil system), **P2** and **P3** were illustrated through the reaction mechanism in Fig. 4 and 6a. The cyclophanediene-based monomer **M1** was first polymerized at 65 °C and initiated through G2 generation in DCE. The reaction progress was monitored using TLC and continued until the complete consumption of **M1** was achieved after 8 hours. At this point, the temperature was gradually lowered to room temperature. Subsequently, the monomer, based on NDIs (**M2** or **M3**), characterized by a higher ring strain than **M1**, was introduced as the exact equivalent of **M1**. Two hours after the addition, the reaction was quenched using EVE and precipitated in methanol; the crude polymers (**P2** and **P3**) were purified by washing several times with methanol and dried. Also, the design of partially rod–coil was obtained *via* random copolymers that were synthesized by copolymerizing **M1** with **M2** to afford **P4** and with **M3** to produce **P5**, as shown in Fig. 4 and 6b. Both copolymerization processes were conducted in the same environment employed for the homopolymer synthesis, **P1**.

Furthermore, the spectroscopic analysis of (**P2–P5**) was confirmed by FTIR data presented in Fig. S12 and S13. Additionally, the ^{1}H-NMR spectrum of (**P2–P5**) indicates that the polymer's microstructure consists of a regular alternating arrangement of *cis* and *trans* configurations, as well as the quantification of *cis*- and *trans*-configurations within the phenylene moieties junctions poses significant challenges. In contrast, norbornene-derived units in **P2**, **P3**, **P4**, and **P5** polymers exhibit defined *cis*-to-*trans* ratios of 52 : 48, 49 : 51, 52 : 48, and 55 : 45, respectively, as determined by rigorous spectral analysis, as shown in Fig. S14 and Fig. S15.

Moreover, Fig. 7 and 8 provide a kinetic study of the resulting polymers (**P2–P5**) that was conducted using ^{1}H-NMR spectroscopy after exposure to UV radiation at a wavelength of 365 nm. A significant alteration in the molecular structure was observed, as evidenced by the shift of the *cis*-configuration signal between phenylene rings from δ 6.45–6.92 ppm to δ 7.15–7.19 ppm in **P2** as a multiple (Fig. 7a) from δ

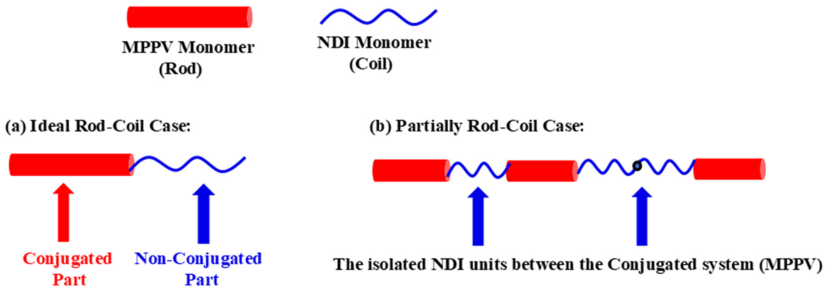

Fig. 6 (a) Block design (**P2** and **P3**), and (b) Random design (**P4** and **P5**).

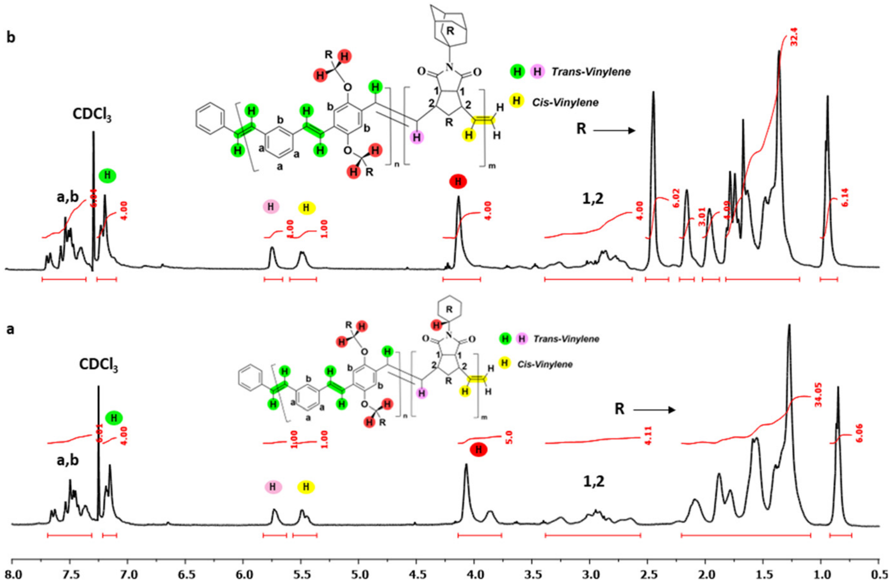

Fig. 7 Spectra of ^{1}H NMR for Ideal Rod-coil Design after photoisomerization under 365 nm(a) poly(DO-MPPV-*co*-CH-NDI) **P2**, and (b) poly (DO-MPPV-*co*-AD-NDI) **P3**.

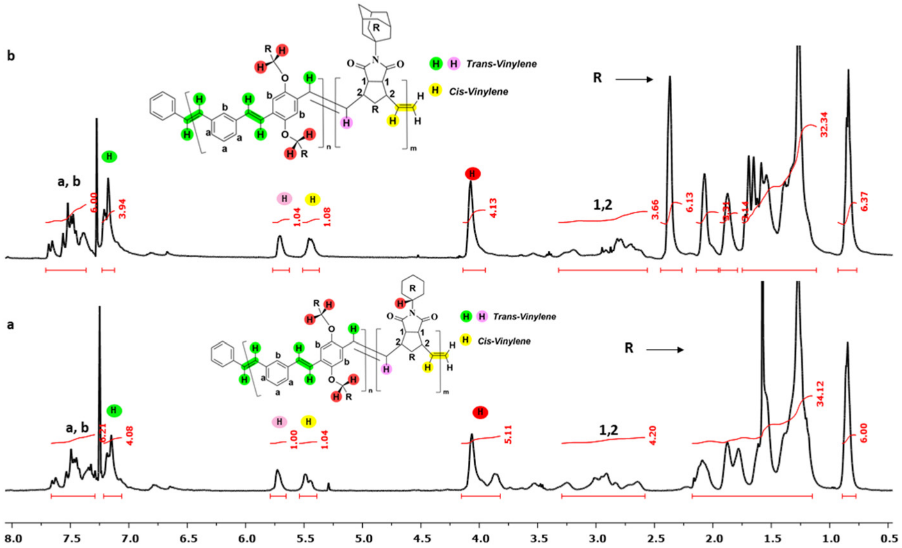

Fig. 8 Spectra of ^{1}H NMR for partially rod–coil design after photoisomerization under 365 nm (a) poly(DO-MPPV-*co*-CH-NDI) **P4**, and (b) poly (DO-MPPV-*co*-AD-NDI) **P5**.

6.41–6.89 ppm to δ 7.17 ppm in **P3** (Fig. 7b), from δ 6.46–6.92 ppm to δ 7.17 ppm in **P4** (Fig. 8a) and from δ 6.45–6.91 ppm to δ 7.077.19 ppm in **P5** (Fig. 8b). This downfield indicates a transition from the *cis* to the *trans* configuration. In contrast, the *cis*-configuration ratios within the *exo*-norbornene units remained unchanged, exhibiting stable values at δ 5.46 ppm for **P2**, δ 5.42 ppm in **P3**, δ 5.48 ppm for **P4**, and δ 5.42 ppm in **P5**, without any transition to their corresponding *trans* signals at δ 5.72, 5.69, 5.70, and 5.70 ppm, respectively. This is attributed to the photostability of the non-conjugated segment of the polymer (such as poly norbornene derivatives), compared to the extended π-conjugated backbone of PPV, which contains photoactive C═C bonds that are susceptible to *cis*–*trans* isomerization under UV irradiation.[51] Additionally, key signals appeared at δ 4.07 ppm in **P2**, **P3**, and **P5** and 3.96 ppm in **P5**, respectively, corresponding to the α-methylene group adjacent to the oxygen atom ($-O\underline{CH_2}-$) within the octyl-substituted phenylene ring. These findings underscore the significant disparity in photostability among the polymeric components governed by their unique chemical structures. Ultimately, the spectral analysis substantiates the formation of a structurally well-defined polymer backbone, consistent with architectures derived from ROMP.

3.3 Temporal kinetics in living ROMP and GPC analysis

The kinetics of metathesis polymerization are pivotal in determining polymer architecture, as the duration of the reaction under the catalytic action of the G2 generation initiator directly influences the molecular weight distribution. This temporal control is especially significant in polymerizing cyclophanediene monomers exhibiting moderate ring strain.[46,52] The influence of polymerization time on molecular weight parameters was systematically investigated by analyzing the weight-average molecular weight (M_w), peak molecular weight (M_p), and number-average molecular weight (M_n) at varying reaction intervals *via* GPC. This analysis was conducted for both homopolymers, such as poly(DO-MPPV), and copolymers, such as poly(DO-MPPV-*co*-CH-NDI) and poly(DO-MPPV-*co*-AD-NDI). As illustrated in Table 1, the GPC analysis of **P1** demonstrates a steady increase in molecular weight distribution (M_p, M_w, and M_n) as polymerization time progresses, culminating in maximum values of 36.64, 33.49, and 37.50 kDa, respectively, at the third reaction stage (t = 6 hours). Additionally, Fig. 9a illustrates that monitoring PDI reveals its highest value of 1.44 during the early stages of polymerization (t = 2 hours), indicating the coexistence of a significant proportion of oligomeric chains and unreacted monomers because the initial rate of the polymerization process is very high. The broader M_w/M_n ratio (PDI) observed at t = 2 hours reflects irregular polymer chain growth during the initial phase.

Table 1 The kinetic time effect and GPC analysis for HOMO-polymer (**P1**)

Time/hours	GPC data				Repeating units
t	M_p/kDa	M_n/kDa	M_w/kDa	PDI[a]	n[b]
2	28.00	24.23	34.84	1.44	52
4	32.64	28.84	36.54	1.27	62
6	36.29	33.49	37.50	1.13	72
8	34.68	29.10	32.21	1.10	63

[a] PDI value was derived from the ratio between the weight-average molecular weight (M_w) and number-average molecular weight (M_n). [b] The observed number of repeating units is derived from the ratio between M_n and the monomer molecular weight (460.70 g mol^{-1}).

As the reaction advances, the PDI undergoes a notable reduction, reaching its narrowest value of 1.1 at the final stage (t = 8 hours), coinciding with the complete consumption of monomers, as confirmed by TLC analysis. This narrowing of the PDI underscores a significant enhancement in the uniformity of polymer chains. These results unequivocally demonstrate that the ROMP method effectively regulates polymer growth, enabling precise control over the polymerization process, as depicted in Fig. 9a. However, a decline in molecular weight distribution (M_p, M_w, and M_n) is observed at this stage, with values decreasing to 34.68, 29.10, and 32.21 kDa, respectively. This reduction in molecular weight observed between 6 and 8 h can be attributed to chain-transfer processes inherent to ROMP, including intermolecular transfer and intramolecular (backbiting) pathway, which redistribute chain lengths and may generate cyclic oligomers.[14,53]

We examine another aspect of the study, which involves random copolymers represented by **P4** and **P5**. These polymers are based on the presence of two different monomers with varying ring strain. One is norbornenes, as **M2** and **M3**, and the other is based on cyclophanediene **M1**. According to the previous studies[46] NDI compounds exhibit a very high ring strain, so they can be polymerized using the least active initiators, such as the first-generation Grubbs catalyst (G1),

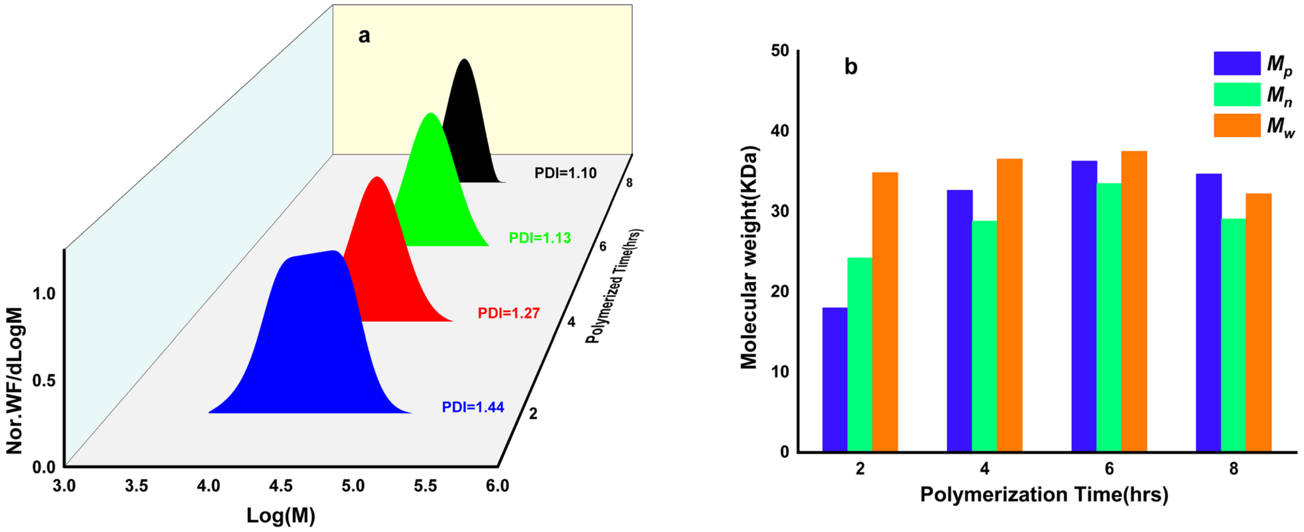

Fig. 9 The relation of the effect of time and (a) PDI and (b) molecular weight distribution for **P1**.

even at room temperature. In contrast, cyclophanedienes cannot be polymerized using G1; instead, the process requires more active initiators, such as G2 or third-generation Grubbs catalysts (G3), or the Hovaydo G2 catalyst, because the ring strain of these materials is moderate compared to the norbornene moieties.[14] Accordingly, these random copolymers were synthesized under the same conditions as **P1** to ensure the polymerization of **M1** through ROMP.

Table 2 presents the GPC analysis results of **P4**, which was obtained from the polymerization of **M1** and **M2**. Upon analyzing PDI values, as shown in Fig. 10a, it was found that they ranged between 1.2 and 1.35. The lowest PDI value of 1.2 was recorded at 2 hours, then increased to its highest value of 1.35 at 4 hours, indicating the polymerization of the monomer with the lower ring strain, cyclopentadiene. After 6 hours of reaction, the PDI value decreased, reaching 1.24, suggesting that the formed polymer chains became more regular. These results were confirmed using **TLC** analysis, which demonstrated that all monomers were wholly consumed, further validating the findings obtained from the GPC analysis.

Furthermore, when analyzing the relationship between reaction time and molecular weight distribution, as illustrated in Fig. 10b, a significant increase in M_p, M_n, and M_w was observed at 18.86, 16.59, and 19.91 kDa. This trend indicates that the polymerization reaction proceeds exceptionally rapidly during its initial stages. This behavior can be attributed to the presence of **M2**, which exhibits high ring strain, making it highly reactive with the ruthenium-based initiator and active site is formed (initiation step), and the polymerization process continues (propagation step), with **M2** playing the dominant role, particularly within the first two hours of the reaction. Despite the continuous increase in molecular weight distribution, the polymerization rate exhibited a noticeable decline compared to the initial stage, particularly during the second and third phases, corresponding to reaction times of 4 and 6 hours, respectively. This reduction can be attributed to the higher consumption of low-strain monomer **M1** than **M2**. Monitoring the reaction *via* TLC during these stages revealed the presence of unreacted monomers, indicating that the reaction had not yet reached completion. Interestingly, after 8 hours—marking the fourth phase—TLC analysis confirmed the complete consumption of all reactants. However, an unexpected and substantial increase in M_p, M_w, and M_n was recorded with values of 103.1193.01 and 74.84 kDa.

Upon GPC analyzing **P5**, as presented in Table 3, which differs from **P4** due to substituting the cyclohexyl group with an adamantyl moiety, a comparative evaluation of their polymerization kinetics revealed notable similarities in behavior. As presented in Fig. 11a, the PDI values for both polymers fluctuated within a range of 1.13 to 1.27 across successive time intervals. Furthermore, the molecular weight distribution steadily increased throughout the first three periods, as shown in Fig. 11b. However, during the 4th stage (t = 8 hours), the reac-

Table 2 The kinetic time effect and GPC analysis for (**P4**)[a]

	GPC data				Repeating units	
Time/hours	M_p/kDa	M_n/kDa	M_w/kDa	PDI[b]	n[c]	m[d]
2	18.86	16.59	19.91	1.20	—	—
4	26.40	25.51	34.48	1.35	—	—
6	30.72	30.89	39.51	1.30	—	—
8	103.11	93.005	74.841	1.24	63	186

[a] **P4** is a random copolymer prepared from polymerized of **M1** and **M2** *via* G2 act as initiator at 65 °C. [b] PDI value was derived from the ratio between M_w and M_n. [c] Number of repeating units derived from **M1** (460.70 g mol^{-1}). [d] Number of repeating units derived from **M2** (245.32 g mol^{-1}).

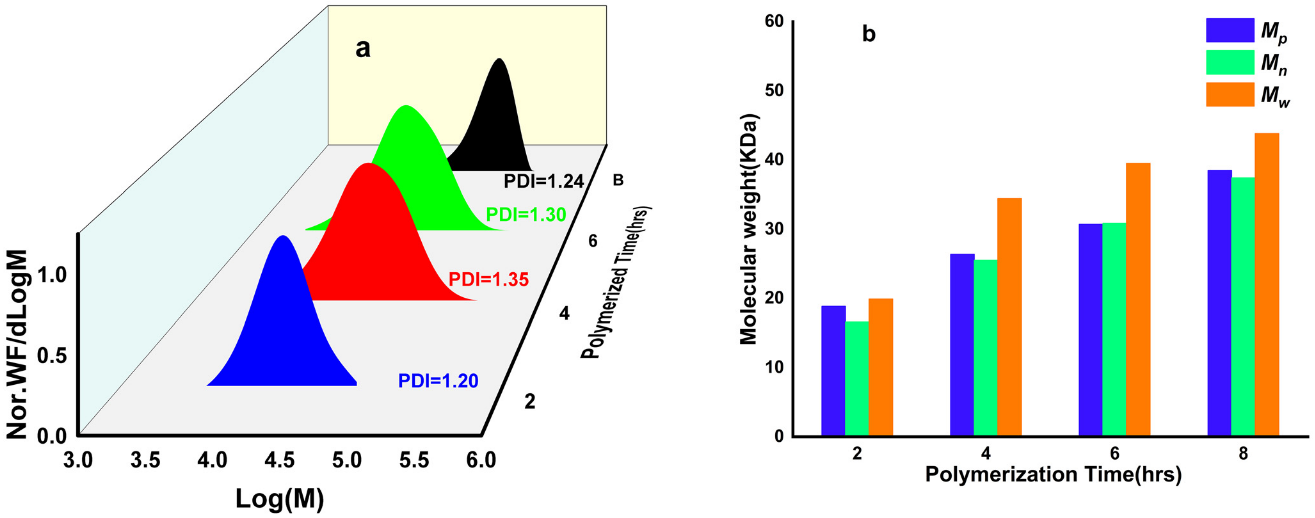

Fig. 10 The relation of the effect of time and (a) PDI and (b) molecular weight distribution for **P4**.

tion rate escalated sharply, leading to a maximum M_p, M_n, and M_w of 51.28, 45.66, and 58.36 kDa, respectively, as all monomeric reactants were consumed entirely. This observation suggests that the elevated reaction temperature at 65 °C, combined with the catalytic activity of the G2 generation catalyst, posed challenges in regulating the polymerization process *via* ROMP. Consequently, these factors may have contributed to unpredictable variations in molecular weight distribution.

In an attempt to control the polymerization process, unlike the previously mentioned random copolymers **P4** and **P5**, copolymers were synthesized using the block approach, as demonstrated in **P2** and **P3**. This method allows precise control over the polymerization temperature of each monomer individually. Such an approach is essential to prevent the uncontrolled increase in molecular weights observed in random **P4** and **P5**, as illustrated in Fig. 12. This diagram highlights two key factors confirming that the ROMP method under these conditions was more effective in controlling the polymerization process. The first factor is the very narrow PDI values, which were 1.14 for **P2** and 1.17 for **P3**, indicating a uniform molecular weight distribution. The second factor is the strong correlation between $M_{n(Obs)}$ and $M_{n(Calc)}$. In **P2**, these values were 35.42 and 35.30 kDa, respectively, while in **P3**, they were 37.10 and 37.91 kDa, as presented in Table 4.

Table 4 summarizes the key findings obtained upon completion of the polymerization reactions, underscoring the critical role of the living ROMP in polymer synthesis. Fig. 12a demonstrates that the homopolymer (**P1**) exhibits the lowest PDI value, 1.1, indicating a high chain regularity. Conversely, the randomly synthesized copolymers (**P4** and **P5**) display significantly higher PDI values (1.24 and 1.27), attributed to the high ring strain of the norbornene moiety and the reaction conditions involving G2 catalyst at 65 °C. Fig. 12b further elucidates the relationship between molecular weight distribution and the synthesized polymers. In block copolymers (**P2** and **P3**), the ROMP method ensured strong agreement between $M_{n(Obs)}$ and $M_{n(Calc)}$, alongside consistent repeating unit counts for **P2** (n = 63; m = 26) and **P3** (n = 63; m = 28). However, randomly, copolymers exhibited marked deviations, particu-

Table 3 The kinetic time effect and GPC analysis for **P5**[a]

Time/hours	GPC data				Repeating units	
t	M_p/kDa	M_n/kDa	M_w/kDa	PDI[b]	n[c]	m[d]
2	18.86	17.21	19.58	1.13	—	—
4	24.09	22.17	25.84	1.66	—	—
6	32.15	29.65	33.70	1.14	—	—
8	51.28	45.66	58.36	1.27	63	66

[a] **P5** is a random copolymer prepared from polymerized of **M1** and **M3** *via* G2 act as initiator at 65 °C. [b] PDI value was derived from the ratio between M_w and M_n. [c] Number of repeating units derived from **M1** (460.70 g mol^{-1}). [d] Number of repeating units derived from **M3** (297.40 g mol^{-1}).

Table 4 GPC analysis for **P1–P5**[a]

Polymer samples	GPC data				Repeating units		
	M_p	M_w	$M_{n(Obs)}$	$M_{n(Calc)}$	PDI[b]	n[c]	m[d]
P1	34.68	32.21	29.10	23.03	1.10	63	0
P2	37.40	40.57	35.42	35.30	1.14	63	26
P3	38.54	43.48	37.10	37.91	1.17	63	28
P4	103.11	93.01	74.84	35.30	1.24	63	186
P5	51.28	58.36	45.66	37.91	1.27	63	56

[a] All polymer samples were synthesized *via* ROMP with G2 generation. [b] PDI value was derived from the ratio between M_w and M_n. [c] Number of repeating units derived from **M1** (460.70 g mol^{-1}). [d] Number of repeating units derived from **M2** (245.32 g mol^{-1}) or **M3** (297.40 g mol^{-1}).

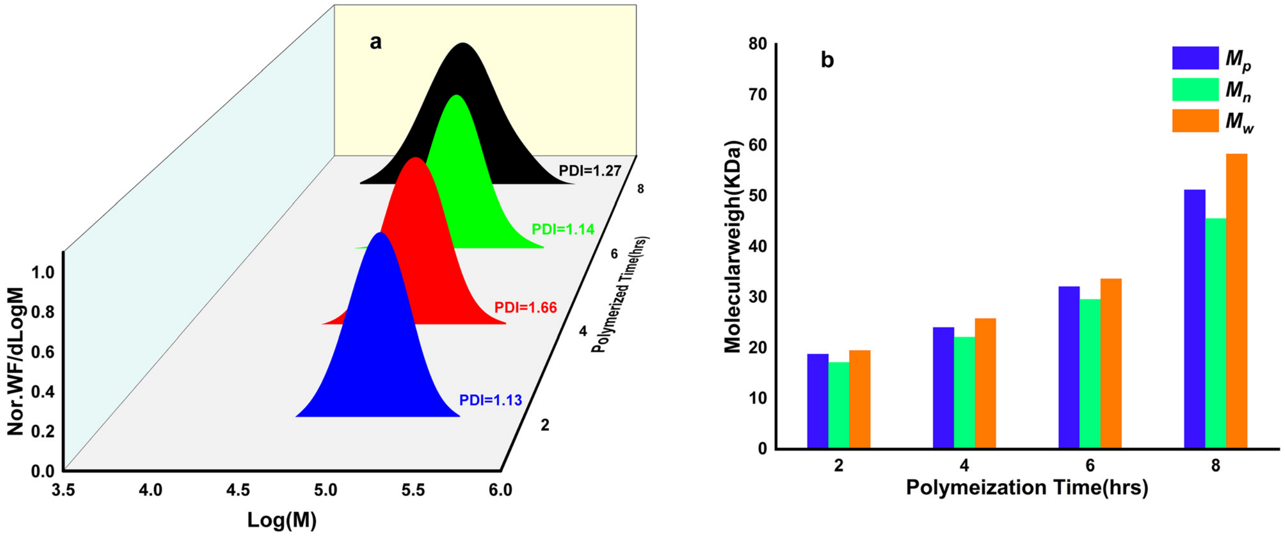

Fig. 11 The relation of the effect of time and (a) PDI, and (b) molecular weight distribution for **P5**.

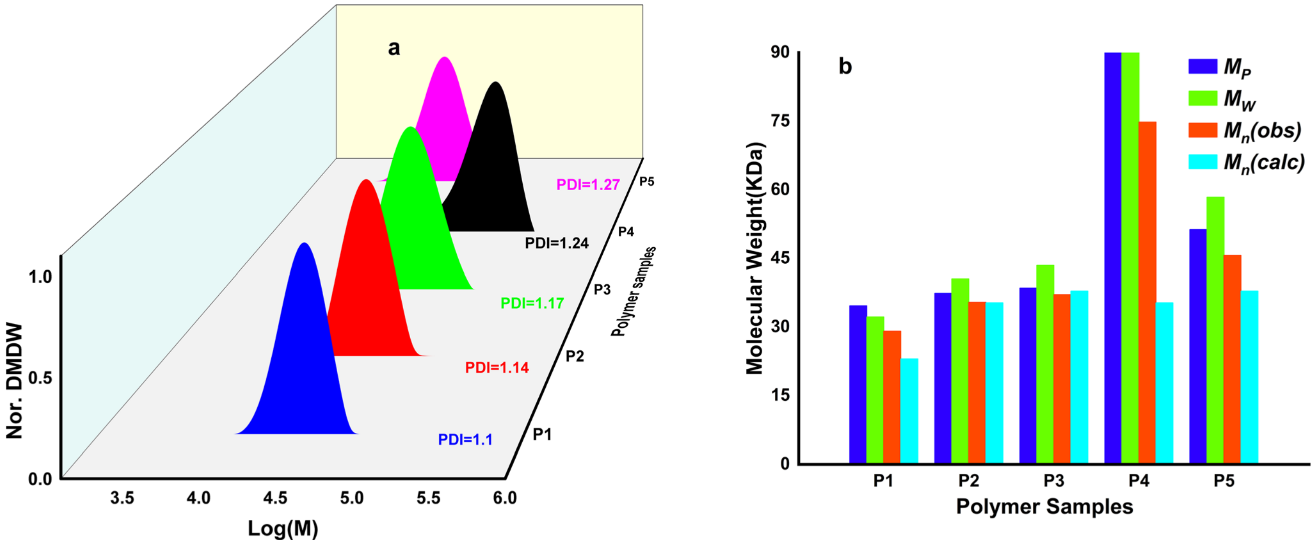

Fig. 12 Synthetic polymers (**P1–P5**); (a) PDI, and (b) comparison of GPC and the theoretical results.

larly in **P4** ($M_{\mathrm{n(Obs)}}$ = 35 kDa; $M_{\mathrm{n(Calc)}}$ = 74 kDa), likely due to polymerization conditions undesirably impacting both PDI and molecular weight distribution. Consequently, block polymerization enabled precise living control over monomer polymerization temperatures.

3.4 Optical properties

The optical properties of both the parent homopolymer (**P1**) and the rod–coil polymers (**P2–P5**) in DCM, mixed solvent (1 : 1; DCM/methanol) solutions, and as thin films were systematically investigated, as illustrated in Fig. 13 and Table 5. In DCM, as provided in Fig. 13a, the results reveal that the fully conjugated homopolymer exhibits the maximum absorption spectrum at $\lambda_{\max}$ 415 nm with band gap E 2.53 eV. In contrast, a slight blue shift was observed in the absorption spectra of the rod–coil polymers, with the shift values measured at 2, 2, 7, and 3 nm for **P2**, **P3**, **P4**, and **P5**, respectively. Additionally, these polymers display two distinct absorption bands, each correlating to specific electronic transitions. The peak at the shorter wavelength is attributed to π–π* transitions, which reflect electronic excitations within the conjugated units. In contrast, the peak at the longer wavelength is associated with intermolecular charge transfer (ICT) between phenylene and vinylene units along the conjugated segments, a phenomenon observed in both the parent homopolymer and the rod–coil polymers.[31,54] The value of λ_{onset} is often defined as the x-intercept of a tangent line on the inflection point for the lowest energy absorption transition of a compound, regardless of whether the lowest energy transition is the highest intensity peak in the spectrum or not.[55] The optical band gap E was investigated using $E_{\mathrm{g}}^{\mathrm{op}} = 1240/\lambda_{\mathrm{onset}}$, and the results indicate that its value ranges from 2.53 to 2.56 eV.

In addition, the absorption spectrum of these polymers was investigated using a micellization protocol based on a 1 : 1 mixture of DCM and methanol Fig. 13b. This solvent system was carefully selected to facilitate micelle formation and stability during spectroscopic measurements. These results were compared with $\lambda_{\max}$ and λ_{onset} obtained from non-

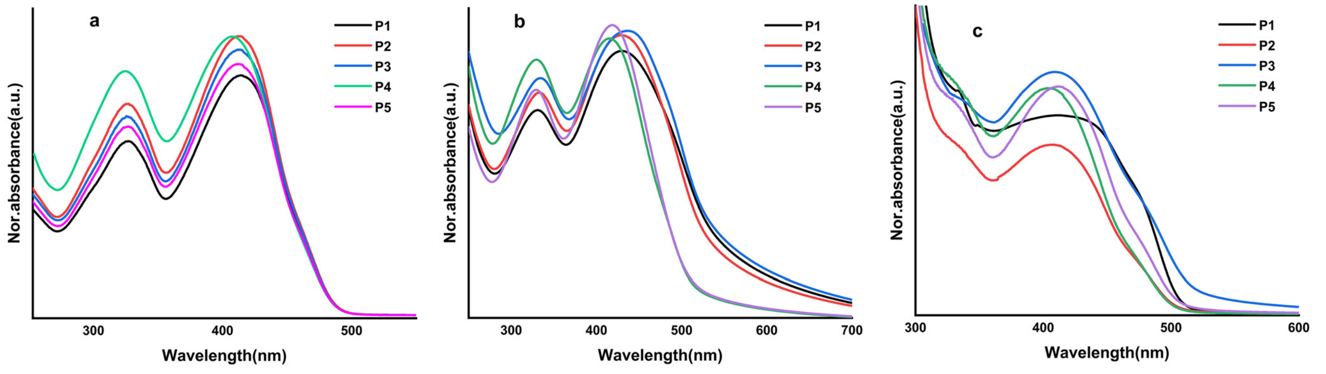

Fig. 13 UV-Vis absorption for the synthetic polymers (**P1–P5**); (a) DCM solvent, (b) micellization protocol, and (c) casting solid-state.

Table 5 UV-Vis absorption for **P1–P5**

	UV-Vis absorption								
	DCM solution			DCM/methanol solution			Thin film		
Polymer samples	$\lambda_{\max}$	$\lambda_{\text{onset}}{}^{a}$	$E_g^{\text{op}}{}^{b}$	$\lambda_{\max}$	$\lambda_{\text{onset}}{}^{a}$	$E_g^{\text{op}}{}^{b}$	$\lambda_{\max}$	$\lambda_{\text{onset}}{}^{a}$	$E_g^{\text{op}}{}^{b}$
P1	415	490	2.53	435	546	2.27	425	508	2.44
P2	413	485	2.55	429	540	2.29	410	504	2.46
P3	413	487	2.54	436	544	2.28	411	517	2.40
P4	408	484	2.56	415	514	2.41	405	501	2.48
P5	412	485	2.55	418	521	2.38	412	508	2.44

[a] λ_{onset} is a tangent line on the inflection point for the lowest energy absorption transition of a compound. [b] The optical band gap (E_g^{op}) was determined *via* the intersection of the tangent on the low-energetic edge of the absorption spectrum with the baseline.

aggregate polymers in DCM solutions, where a significant redshift of 7 to 23 nm in $\lambda_{\max}$ and approximately 30 to 57 nm in λ_{onset} was observed. Additionally, a clear inhomogeneous broadening of the spectra was noted with lower E_g^{op} ranging from 2.27–2.41 eV, which is likely attributed to solvent interactions at the interface of polymers, along with variations in internal molecular arrangement and molecular aggregation resulting from the addition of a polar solvent such as methanol. The redshift effect was most prominent in the parent polymer (poly(DO-MPPV)) due to its fully conjugated chain structure, which facilitates enhanced electron transfer along the polymer chain. In contrast, the random copolymer exhibited a smaller redshift in values 6 and 7 nm for **P4** and **P5**, respectively, due to the irregular distribution of the conducting PPV units, which are isolated by the non-conducting norbornene units, disrupting the electronic conjugation on the polymer backbones. Furthermore, in the block copolymer case, the redshift was comparable to that observed in the fully conjugated polymer, suggesting improved electron transfer and better molecular organization. These findings are consistent with the unit count obtained from the GPC analysis Table 4, further confirming the influence of molecular structure on the spectral properties of the studied polymers.

On the other hand, a primary and distinct absorption band was observed after analyzing the solid-state thin film's absorption spectrum, as depicted in Fig. 13c. However, this band appeared broader than its counterpart in solution and micellization protocol, which can be attributed to molecular aggregation effects in the solid state. The recorded $\lambda_{\max}$ ranged from 405 to 425 nm. These findings indicate that the parent polymer **P1** underwent a bathochromic shift of 10 nm. In contrast, the other rod–coil polymers exhibited nearly identical $\lambda_{\max}$ compared to their solution-phase counterparts. A shoulder peak was also detected at 478 nm, further indicating intermolecular interactions and aggregation phenomena. Furthermore, the onset wavelength λ_{onset} values used to estimate E_g^{op} were 508 nm for **P1** and **P5**, 504 nm for **P2**, 517 nm for **P3**, and 501 nm for **P4**. Consequently, the band gap values in the solid state were lower than those in the solution, ranging from 2.40 to 2.48 eV, as presented in Table 5. This reduction is primarily attributed to molecular aggregation and enhanced orbital overlap in the solid state, facilitating electronic transitions at lower energy levels.

3.5 Thermal properties

This study is underpinned by a meticulous evaluation of the thermal stability of polymers, a process that plays a vital role in understanding their physical and mechanical properties. We employed the rigorous techniques of Thermogravimetric Analysis (TGA) and Differential Scanning Calorimetry (DSC) under environmental nitrogen to ensure the accuracy of our findings. TGA was performed to assess the thermal stability of the parent polymer (**P1**) and the rod–coil polymers (**P2–P4**). These results were carried out on the *trans* polymer after photoisomerization under 365 nm UV irradiation and are provided in Fig. 14 and summarized in Table 6. The polymers studied exhibit significant thermal stability, with onset decomposition temperatures (T_d^{onset}) ranging from 368 °C to 395 °C, alongside a weight loss percentage of approximately 2–5%. Furthermore, the residual weight, which varies from 17% to 25% after heating up to 800 °C, can be attributed to the presence of aromatic rings in the PPV units, as highlighted in Table 6. This remarkable thermal stability is likely due to the decomposition of the octyl side chains connected to the benzene rings within the polymer backbone.

As illustrated in Fig. 14A, the thermal stability of the fully conjugated polymer (**P1**) exhibits T_d^{onset} of 368.2 °C, which is lower than the corresponding temperatures observed for the rod–coil type polymers (**P2–P5**). The incorporation of norbornene moieties, specifically CH-NDI and AD-NDI, in both random and block copolymers, which are recognized for their high thermal stability,[13] was intended to enhance the thermal stability of (PPV) derivatives. This enhancement is apparent in the performance of polymers **P2**, **P3**, **P4**, and **P5**, which exhibit T_d^{onset} of 382.6 °C, 392.7 °C, 386.2 °C, and 394.6 °C, respectively, as shown in Fig. 14(B–E). Moreover, the excellent thermal stability results obtained indicate that these polymers can resist morphological deformation in the active layer films prepared from them when subjected to electric fields.[56,57] This enhances their potential for use in optoelectronic applications.[2,6,13,31,56]

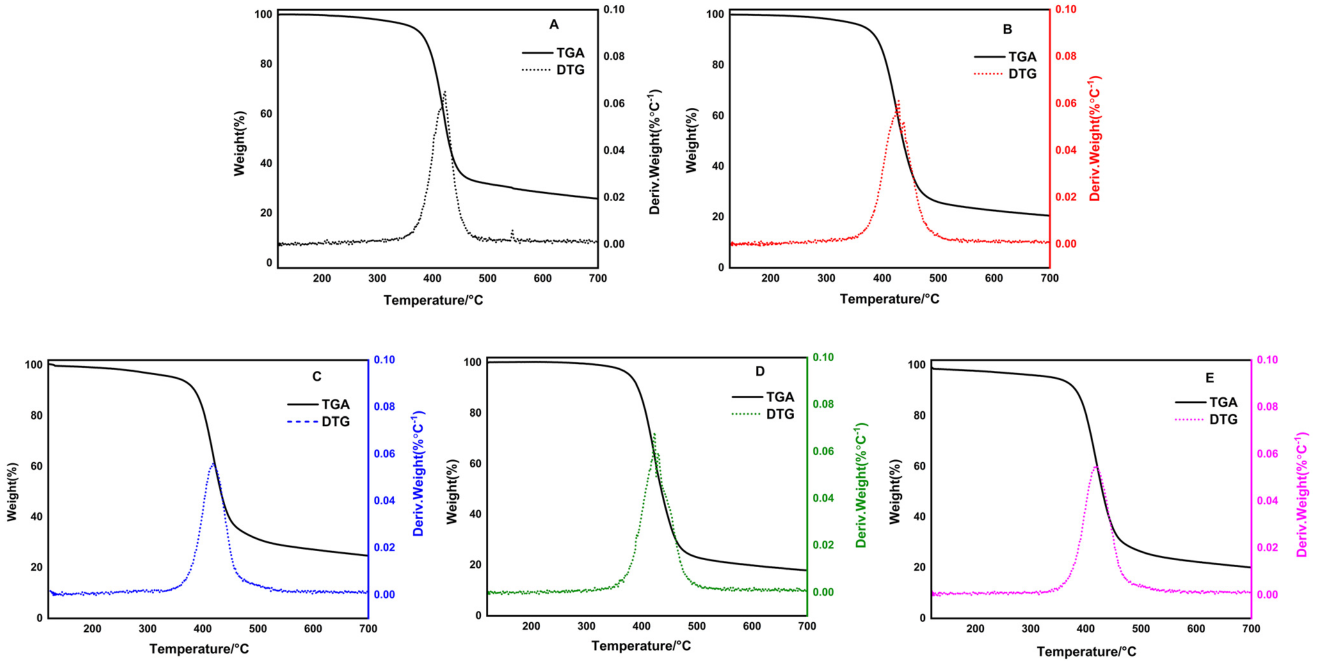

Fig. 14 TGA and DTG-curves for the synthetic polymers: A (**P1**), B (**P2**), C (**P3**), D (**P4**), and E (**P5**).

Table 6 Data of the HOMO and copolymers

Polymer samples	T_d^{onset} [a]	wt loss[a] (%)	DTG[a]	Residual[a] (%)	T_g [b]
P1	368.2	3.0	422.1	25.8	108.4
P2	382.6	3.7	430.0	20.2	161.8
P3	392.7	5.1	418.0	24.3	167.3
P4	386.2	1.9	424.0	17.7	172.9
P5	394.6	5.4	419.0	19.7	176.5

[a] TGA analysis was performed in a nitrogen atmosphere with a heating rate of 10 °C per minute. [b] DSC analysis was performed in a nitrogen atmosphere with a heating rate of 10 °C per minute.

The polymer samples were carefully heated to 300 °C, and the DSC data obtained from the second heating scan, as presented in Table 6, are a testament to the thoroughness of our research. The DSC curve shown in Fig. S16, a key aspect of this protocol, indicates that the glass transition temperature (T_g) values range between 108.4 °C and 176.5 °C. The parent polymer (fully conducting) exhibited the lowest T_g, measuring 108.4 °C, compared to the polymers synthesized using the rod–coil system *via* copolymerization of **DO-*mp*-CPDE** (**M1**) with norbornene derivatives as CH-NDI (**M2**) or AD-NDI(**M3**). These copolymers significantly increased T_g, ranging from 53.4 °C to 68.1 °C. This trend suggests that polymers incorporating norbornene units inherently show higher T_g values. To further clarify, a comparison between block copolymers (**P2** and **P3**) and random copolymers (**P4** and **P5**) reveals that the T_g values of **P2** and **P3** (completely rod–coil) are lower than those of **P4** and **P5** (partially rod–coil), respectively. This difference can be attributed to the number of norbornene units incorporated during polymerization. GPC data confirm that the partial rod–coil contains a higher fraction of norbornene units than the ideal rod–coil, which accounts for their elevated T_g values, 172.9 °C for **P4** and 176.5 °C for **P5**, compared to the block copolymers (which exhibit T_g values 161.8 °C and 167.3 °C for **P2** and **P3**, respectively).

3.6 Electrochemical properties

Studying the electrochemical properties *via* cyclic voltammetry (CV) presents valuable insights into the electronic energy levels of the prepared samples. Understanding these levels is vital for calculating the electrochemical bandgap (E_g^{elc}), which plays a significant role in their applications in electronic devices. Fig. 15 provides the oxidation and reduction potentials for each polymer. From these potentials, we calculated the highest occupied molecular orbital (HOMO) and lowest unoccupied molecular orbital (LUMO) values, which indicate the ionization potential and electron affinity, respectively.

The CV was performed on the parent polymer **P1** and the rod–coil polymers (**P2–P5**). The working electrode was prepared by drop-casting a tetrahydrofuran (THF) solution onto indium tin oxide (ITO) glass, which was then dried for 12 hours at 40 °C. This process utilized (0.1 M) a solution containing tetrabutylammonium hexafluorophosphate (TBAPF$_6$) in an anhydrous acetonitrile, which acts as the supporting electrolyte. The CV measurements were conducted at a scan rate of 20 mV s^{-1}. Table 7 shows the onset oxidation (E_{onst}^{oxi}) and onset reduction potentials (E_{onst}^{red}) of the synthesized polymers, the E_{onst}^{oxi} were found to range from 0.92 to 1.35 V, while the E_{onst}^{red} ranged from −1.02 to −1.09 V, as well as the energy

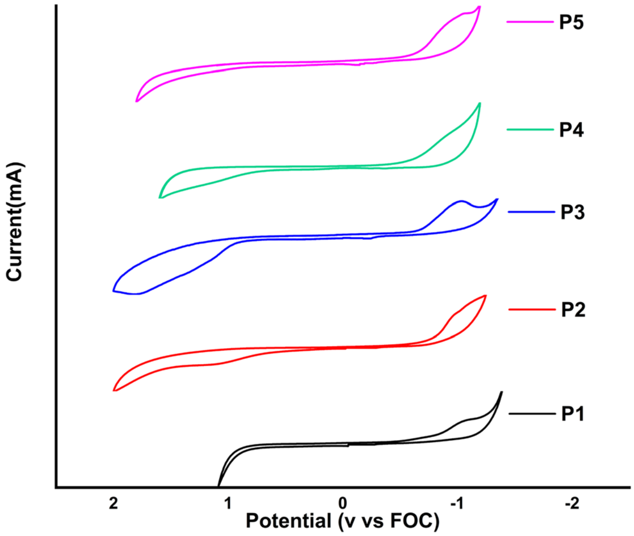

Fig. 15 CV-curve for the synthetic polymers (**P1–P5**), US convention.

Table 7 CV data of the HOMO and block copolymers

Polymer samples	$E_{\text{onst}}^{\text{red}}$ *vs.* FOC[a]	$E_{\text{onst}}^{\text{oxi}}$ *vs.* FOC[a]	E_{LUMO}[b] (eV)	E_{HOMO}[b] (eV)	$E_{\text{g}}^{\text{elc}}$[b] (eV)
P1	−1.09	0.92	−3.71	−5.72	2.01
P2	−1.08	1.29	−3.72	−6.09	2.37
P3	−1.04	1.12	−3.76	−5.92	2.16
P4	−1.02	1.35	−3.78	−6.15	2.37
P5	−1.05	1.21	−3.75	−6.01	2.26

[a] E_{FOC} = 4.8 V *vs.* $AgNO_3$. [b] Calculated from eqn (1)–(3), respectively.

levels of the HOMO (E_{HOMO}) and LUMO (E_{LUMO}), which were calculated using eqn (1) and (2), respectively.

$$E_{\text{HOMO}} = -e\left(4.8 + E_{\text{onset}}^{\text{oxi,FOC}}\right) \tag{1}$$

$$E_{\text{LUMO}} = -e\left(4.8 + E_{\text{onset}}^{\text{red,FOC}}\right) \tag{2}$$

$$E_{\text{g}}^{\text{elc}} = E_{\text{LUMO}} - E_{\text{HOMO}} \tag{3}$$

The values of E_{HOMO} and E_{LUMO} for each polymer were as follows: E_{HOMO} – **P1:** −5.72, **P2:** −6.09, **P3:** −5.92, **P4:** −6.15, and **P5:** 6.01; E_{LUMO} – **P1:** −3.71, **P2:** −3.72, **P3:** −3.76, **P4:** −3.78, and **P5:** −3.75. In addition, the $E_{\text{g}}^{\text{elc}}$ was calculated using the difference between the energy values of E_{HOMO} and E_{LUMO} as provided in eqn (3), where their values ranged from 2.01 to 2.37 eV. The results show that the parent polymer (**P1**) exhibits the narrowest $E_{\text{g}}^{\text{elc}}$ value of 2.01 eV among all the polymers, indicating its superior performance due to being a fully conjugated system. For the copolymer results, we notice a slight increase in the $E_{\text{g}}^{\text{elc}}$ values in both block **P2** and **P3** and random copolymer **P4** and **P5**, with values ranging from 0.15 to 0.36 eV. This is due to the presence of non-conductive units such as CH-NDI and AD-NDI, which are connected to the conductive PPV units. This increase can be attributed to the presence of non-conductive units like CH-NDI and AD-NDI, which are integrated with the conductive PPV units, leading to the observed bandgap values.

3.7 Morphology studies

SEM analysis was performed on polymer thin films prepared by two different protocols to investigate the effect of solvent environment on film morphology, as illustrated in Fig. 16. The protocol (A) involved casting the polymer from a pure tetrahydrofuran (THF) solution, while the protocol (B) utilized a micellization method involving a THF/methanol mixture. The films prepared from pure THF solution (protocol A) exhibit a relatively smooth and homogeneous surface morphology. This is attributed to the high solubility of the polymer in THF, which results from the presence of octyl side chains, which facilitate uniform distribution of the polymer chains during film formation and effectively prevent large-scale aggregation or clustering within the structure.

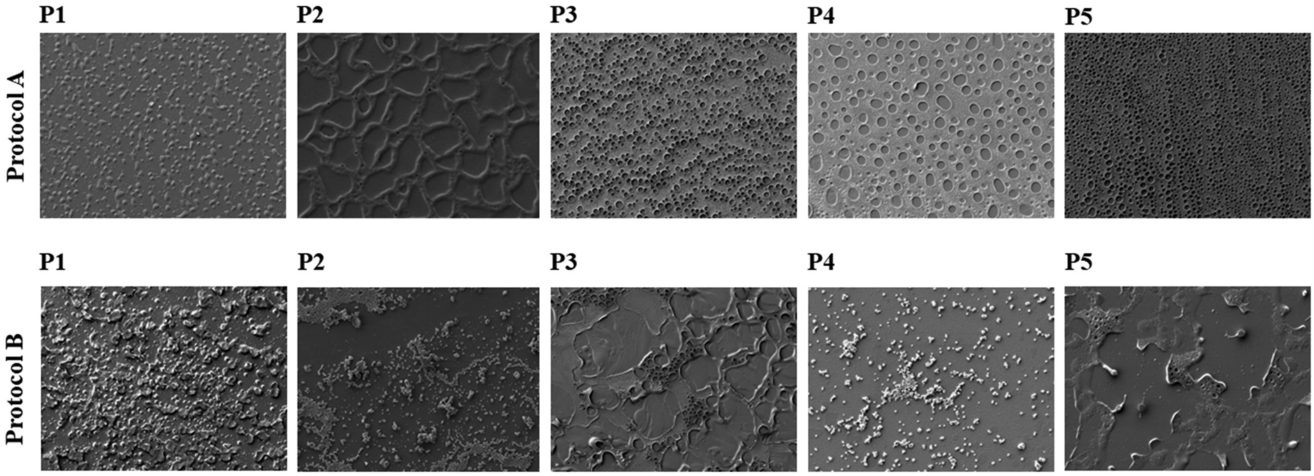

Fig. 16 SEM morphology analysis of polymer thin films (**P1–P5**) from two protocols: (A) casting from pure THF and (B) casting from micellization system THF/MeOH.

In the case of the homopolymer (**P1**), the morphology consists of nearly homogeneous spherical particles with an average diameter of approximately 3.8 µm. On the other hand, the copolymers formed by linking norbornene units with PPV segments exhibit morphologies characterized by well-defined cavity structures. These features appear consistently in both the block (**P2** and **P3**) and random (**P4** and **P5**) copolymers, with only slight variations in particle diameter. The average diameters of these structures are approximately 7.5 µm for **P2**, 2.55 µm for **P3**, 9.5 µm for **P4**, and 1.9 µm for **P5**, respectively. In contrast, the films prepared in accordance with protocol B have a notably different morphology that is distinguished by the existence of phase-separated or aggregated domains. Methanol's poor solvating ability for the polymer is the cause of this structural variation.

In this context, polymers **1**, **2**, and **4** display closely packed spherical particles with average diameters of approximately 4.2, 2.7, and 1 µm, respectively. On the other hand, polymers **3** and **5** show irregular morphologies with average diameters of 34.1 µm for polymer **3** and 13.2 µm for polymer **5**, with noticeable porous features, where the average pore diameters reach 4.7 µm for polymer 3 and 4.2 µm for polymer **5**. These SEM-observed structural characteristics align with the UV-Vis absorption results, which show spectral shifts suggestive of polymer aggregation. Significantly, as shown in the accompanying Fig. 13b, a bathochromic shift (redshift) in the absorption peaks was found.

3.8 DFT study

The Density functional theory was used to get a deeper insight into the polymer's electronic structures and polymerization patterns. The software Avogadro 1.2.0 was used to sketch the 3D models of the polymers, followed by pre-optimization using the MMFF94 force field.[58] Then, using the ORCA 6.0.1 software,[59–63] structures were further optimized using B3LYP,[64] since it offers a good balance between calculation speed and accuracy of the results,[65,66] with RIJCOSX approximation to reduce the computational cost, and using the basis set 6-31++G(d,p). The geometry optimization convergence for energy change, RMS gradient, max gradient component, RMS displacement, and max displacement were set to 5×10^{-6} Eh, 1×10^{-4} Eh per Bohr, 3×10^{-4} Eh per Bohr, 2×10^{-3} Bohr, and 4×10^{-2} Bohr, respectively. The HOMO and LUMO were obtained, and the energy gap was calculated.[67,68] For the TD-DFT calculations to get the UV-Vis spectra of the investigated polymers, the CAM-B3LYP functional was used.[69,70] The optimized structure from the first calculations by B3LYP/6-31++G(d,p) was introduced into the TD-DFT calculation using CAM-B3LYP functional with RIJCOSX approximation and the same basis set. The maximum dimension of the subspace used in each iteration was set to 5, and the number of roots was set to 30. The solvent model used in the TD-DFT calculations is the Conductor-like Polarizable Continuum Model (CPCM), which is implemented in ORCA software, and the solvent used is dichloromethane (DCM).

To understand the electronic structure of the synthesized polymers and to have a better look at the pattern of polymerization, the density functional theory was used. The long octyl chain of (DO-MPPV) is replaced by a methyl group to reduce the computational cost. This substitution has neither a noticeable effect on the frontier molecular orbitals (HOMO and LUMO) energies nor a significant effect on UV-Vis Spectra, since its alkane chains do not contribute to the conjugation of the polymer.[71,72] A 3D sketch of the models used in DFT calculations is shown in Fig. 17. The results of DFT calculations for the synthesized polymers are tabulated in Table 8 along with the experimental results obtained from the UV-Vis spectroscopy and cyclic voltammetry measurements. The Frontier Molecular Orbitals (FMO) from the DFT calculations and the twisting angles are shown in Table 9 and Fig. S17, respectively. The observations that can be noticed in the values of the energy gaps are that the energy gaps obtained from the DFT calculations are higher than those obtained from experimental means, as shown in Fig. 18. This can be attributed to the fact that the DFT calculations are carried out using a single molecule in vacuum, which leads to the overestimation of energy gaps. This reason holds for both UV-Vis spectroscopy measurements and Electrochemical measurements. When the UV-Vis spectroscopy is considered alone, another stability factor is responsible for the decrease in the observed energy gap, which is the exciton effect. When the electron is excited into a higher energy level, it leaves behind a positive hole, which leads to a coulombic attraction that gives stability to the molecule in the excited state and is reflected in the low observed energy gap. When the electrochemical measurement is considered alone, the condensed molecules in the film and the solvent effects must be taken into consideration, which contribute to lowering the experimental energy gap.[73,74]

The theoretical UV-Vis spectra of the investigated polymers were analyzed and compared with the experimental ones in DCM solvent, as shown in Fig. 19, and the resulting data are tabulated in Table 10. It was found that for the first polymer, **P1**, an excellent agreement was observed in the TD-DFT spectrum with the experimental result. The maximum wavelength from the TD-DFT is 400.04 nm, which is very close to the experimental value of 415 nm. This confirms the formation of the polymer **P1** and its structure.

For polymers, **P2** and **P3**, a noticeable deviation between the maximum wavelength obtained from the theoretical results and the experimental results. The theoretical maximum wavelengths of **P2** and **P3** are 393.11 nm and 393.01 nm, respectively, while the experimental results are 413 nm for both polymers. The same deviation is observed in **P4** and **P5**. The theoretical maximum wavelengths of **P4** and **P5** are 355.14 nm and 355.56 nm, respectively, while the experimental results are 408 nm and 412 nm, respectively.

These results lead to the conclusion that for the block polymer (**P2** and **P3**) and random polymer (**P4** and **P5**), the electrochemical and optical behavior is similar to that of **P1** due to reaching the effective conjugation length. The detailed explanation behind this conclusion is based on the observations from the synthesis step, together with UV-Vis spectroscopy and DFT calculations. It was noted that the polymer-

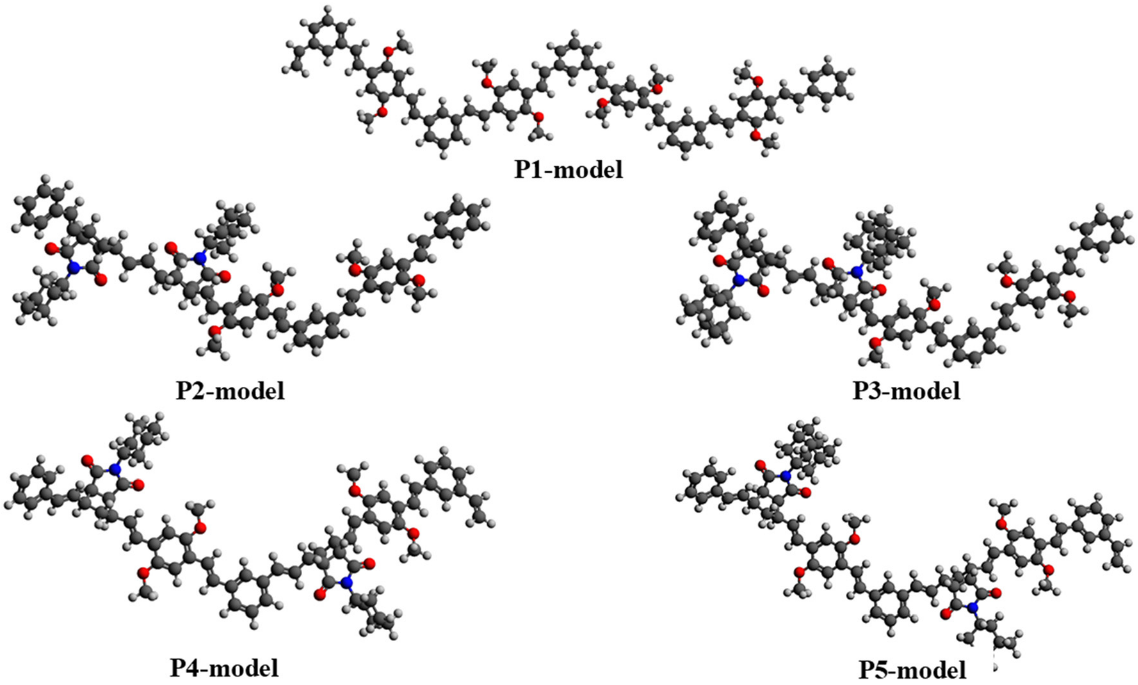

Fig. 17 A 3D sketch of the models used in the DFT study.

Table 8 The DFT results using B3LYP/6-31++G(d,p) together with the experimental results of UV-Vis spectroscopy and cyclic voltammetry

	DFT calculations			UV-Vis spectroscopy		Cyclic voltammetry		
Polymer	HOMO (eV)	LUMO (eV)	E_g^{th} (eV)	E_g^{op} (eV) (solv. DCM)	E_g^{op} (eV) (film)	HOMO (eV)	LUMO (eV)	E_g^{elc} (eV)
P1	−5.000	−2.022	2.978	2.53	2.44	−5.72	−3.71	2.01
P2	−5.007	−1.967	3.040	2.55	2.46	−6.09	−3.72	2.37
P3	−5.006	−1.965	3.041	2.54	2.40	−5.92	−3.76	2.16
P4	−5.106	−1.750	3.356	2.56	2.48	−6.15	−3.78	2.37
P5	−5.099	−1.750	3.349	2.55	2.44	−6.01	−3.75	2.26

ization of conjugated monomers (**DO-*mp*-CPDE**) to synthesize **P1** took about 8 hours to be completely consumed. In contrast, the polymerization of the non-conjugated monomers (CH-NDI and AD-NDI), leading to **P2–P5**, was achieved within a considerably shorter period, which can be attributed to the higher ring strain present in CH-NDI and AD-NDI.[40,75] This indicates the higher kinetics of non-conjugated monomers compared to the conjugated monomers. For **P2** and **P3**, the conjugated **DO-*mp*-CPDE** monomers are already gathered together at the first step of synthesis to form a homopolymer chain followed by addition of the non-conjugated monomers (CH-NDI) and (AD-NDI) at the terminal of the polymer chains which means that both polymer chains have segments that reach the effective conjugation length as shown in Fig. S18(a) and Table 11.

For **P4** and **P5**, and based on the fast kinetic observation of the non-conjugated monomers due to high ring strain,[40] it is reasonable to predict that polymerization initiates with the faster-reacting monomers, *i.e.*, (CH-NDI) for **P4** and (AD-NDI) for **P5**, interspersed with some units of DO-*mp*-CPDE. After the consumption of fast kinetic polymerization monomers, the remaining **DO-*mp*-CPDE** monomers shall polymerize at the terminal of the formed random chains and reach the effective conjugation length as shown in Fig. S18(c) and Table 11.

UV-Vis measurements were used to prove this assumption. It was noted that the UV-Vis spectrum of the five synthesized polymers exhibits nearly the same λ_{max} values and the same optical band gaps, although the synthesis procedures were different and the components of the polymers were different. **P1** is fully composed of conjugated monomers, whereas **P2–P5** incorporate non-conjugated monomers. This similarity in optical properties suggests that the five polymers have attained the effective conjugation length, resulting in similar absorption maxima.[76]

Further confirmation was obtained through DFT calculations. Among the five DFT models, it was noted that the model with the UV-Vis spectrum that resembles the experimental one is the model that has four conjugated monomers of **P1**. Decreasing the number of conjugated monomers, as in the **P2** and **P3** models, decreases the λ_{max}. It was noted that

Table 9 The FMOs of the optimized polymer structures using B3LYP/6-31++G(d,p)

	HOMO	LUMO
P1	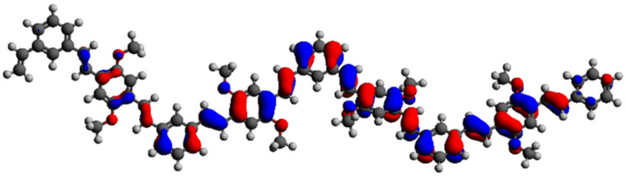	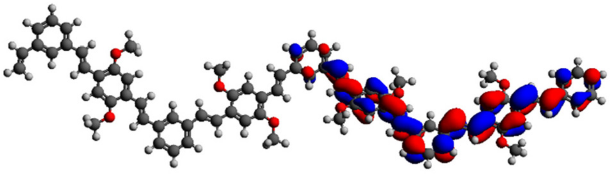
P2	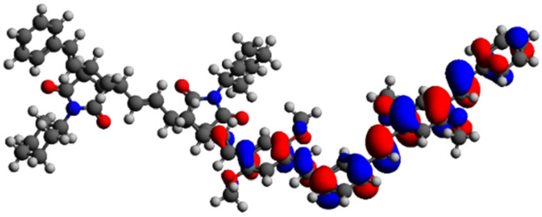	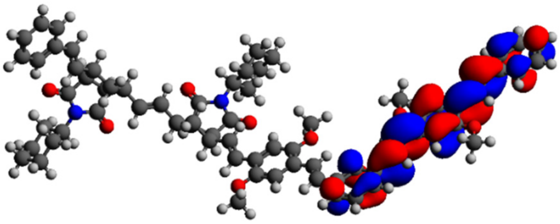
P3	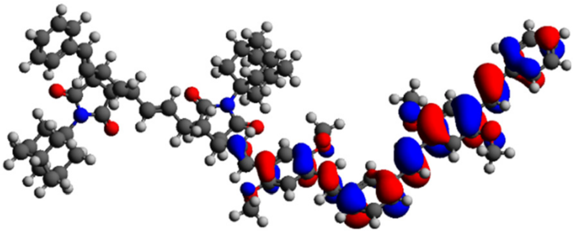	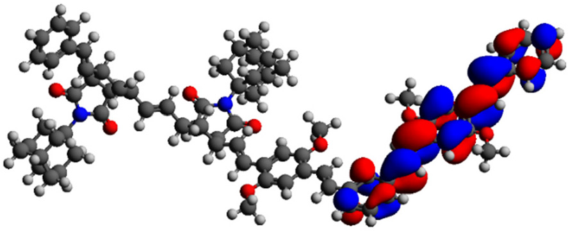
P4	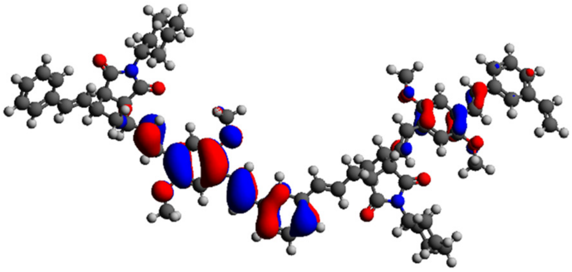	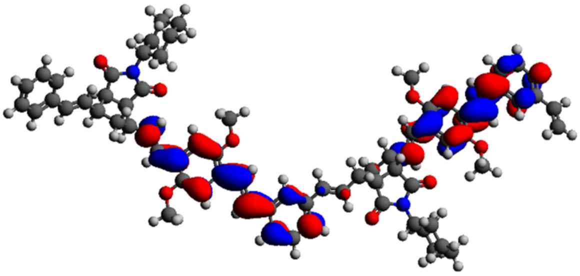
P5	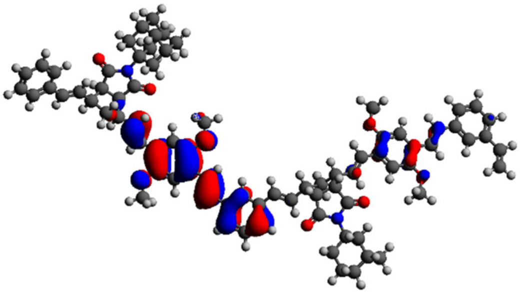	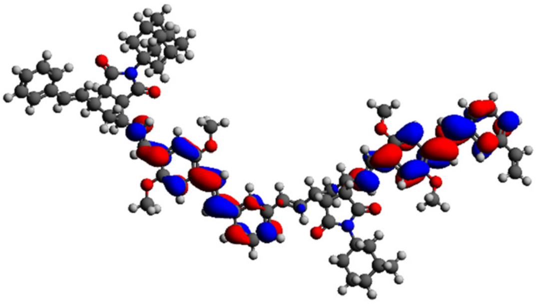

$\lambda_{\max}$ further decreases when these monomers are separated from nonconjugated monomers. These results, together with the increment observed in the theoretical energy gap from Table 8 and Fig. 18 that have the order **P4** ≈ **P5** > **P3** ≈ **P2** > **P1**, and comparing it with the experimental energy gaps are nearly the same, implies that in order for the five polymers to have the same UV-Vis spectrum and HOMO–LUMO gaps, aggregated conjugated monomers that have reached effective conjugated length should be present. For the **P4** and **P5**, this means that the polymerization was not quite random, as shown in Fig. S18(b), but instead it has **DO-*mp*-CPDE** segments that reached the effective conjugation length, as shown in Fig. S18(c).[77,78]

To evaluate the synthesized polymers' feasibility for BHJ organic solar cells, density functional theory (DFT) calculations were used to compare the frontier molecular orbitals

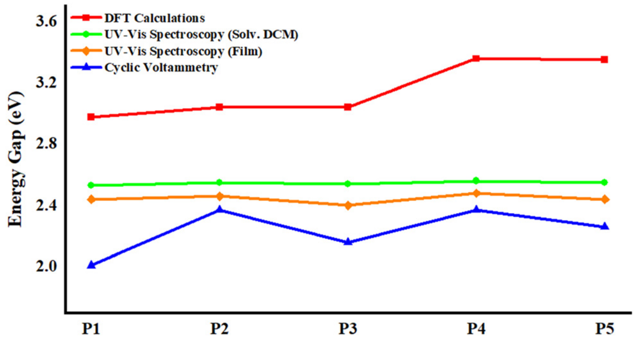

Fig. 18 The energy gaps were obtained from the different methods used in the present study.

(FMOs) of the polymers (**P1–P5**) with those of [6,6]-phenyl-C_{61}-butyric acid methyl ester (PCBM). BHJ devices usually consist of a fullerene derivative as the electron acceptor and a π-conjugated copolymer as the electron donor. It has been demonstrated that PCBM's cage-like, three-dimensional construction facilitates effective energy storage and photovoltaic conversion.[60]

After carrying out geometry optimization to the PCBM's structure at the DFT/B3LYP/6-31++G(d,p) level, as shown in Fig. 20, the lowest unoccupied molecular orbital (LUMO) was compared with those of the synthesized polymers (**P1–P5**). The LUMO offset between each polymer and PCBM, in particular, varies between 1.337 and 1.609 eV, suggesting that photo-excited electron transport to PCBM could be sufficiently efficient to be utilized in photovoltaic cells. The power conversion efficiency (PCE) of the latter could be computed using:

$$\mathrm{PCE}(\%) = \frac{J_{\mathrm{SC}} \times V_{\mathrm{OC}} \times \mathrm{FF}}{P_{\mathrm{m}}} \times 100\%$$

where FF stands for fill factor, (V_{OC}) for open-circuit voltage, J_{SC} for short-circuit current, and P_{m} for incident power density. Considering energy loss during photo-charge generation, the BHJ solar cell's maximum open-circuit voltage (V_{OC}) is correlated with the difference between the HOMO of the electron-donating polymer and the LUMO of the electron-accepting full-

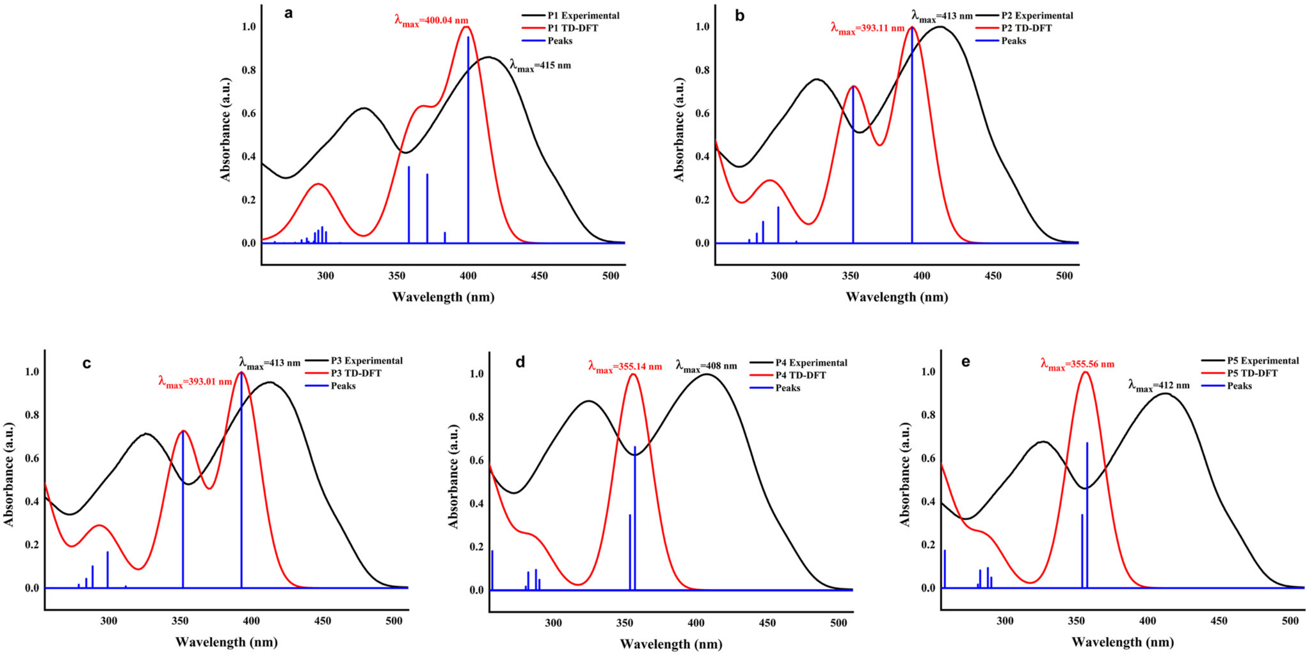

Fig. 19 The experimental UV-Vis spectra of **P1** (a), **P2** (b), **P3** (c), **P4** (d), and **P5** (e) with those obtained from the TD-DFT using CAM-B3LYP/6-31++(d,p)G.

Table 10 The maximum wavelengths, energies, oscillator strengths, and the major contributing orbital pairs in the excitation for **P1–P5** obtained from TD-DFT using CAM-B3LYP/6-31++(d,p)G

Polymer	$\lambda_{\max}$ (nm)	*E* (eV)	Oscillator strength (f)	Major contributing orbital pairs in the excitation
P1	400.04	3.099	4.609	**H → L+2** (30.25%), **H−2 → L** (21.82%), **H−3 → L** (10.37%)
P2	393.1	3.154	2.019	**H → L** (75.03%)
P3	393.0	3.155	2.024	**H → L** (74.46%)
P4	357.1	3.472	2.173	**H−1 → L** (30.67%), **H−1 → L+1** (16.17%), **H → L** (13.93%), **H → L+1** (31.22%)
P5	357.5	3.468	2.219	**H−1 → L** (32.85%), **H−1 → L+1** (14.87%), **H → L** (10.68%), **H → L+1** (33.57%)

Table 11 A comparison between the pattern of DFT models and the actual pattern of polymerization, where A = DO-MPPV, B = CH-NDI, and C = AD-NDI, and the calculated maximum open-circuit voltage from the DFT using B3LYP/6-31++(d,p)G

Polymer	Pattern of DFT model	Actual pattern of polymerization	V_{OC}
P1	AAAA	AAAAAAAAAAAAAAAAAAAAAAAAAAAAA	1.341
P2	AA-BB	AAAAAAAAAAAAAA-BBBBBBBBBBBBBBB	1.348
P3	AA-CC	AAAAAAAAAAAAAA-CCCCCCCCCCCCCC	1.347
P4	B-A-B-A	BBB-AAA-BBBB-AA-BB-AAAA-BBB-AAAAAAAAA	1.447
P5	C-A-C-A	CCC-AAA-CCCC-AA-CC-AAA-CCC-AAAAAAAAA	1.440

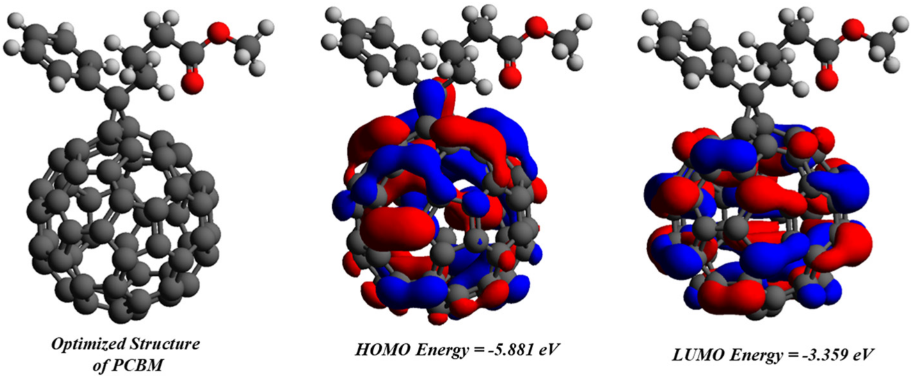

Fig. 20 The optimized structure of PCBM using B3LYP/6-31++(d,p)G and its frontier orbitals HOMO and LUMO.

erene. The open-circuit voltage (V_{OC}) values have been computed using the following formula:

$$V_{OC} = \frac{1}{e}\left[\left|E_{HOMO}^{Donor}\right| - \left|E_{LUMO}^{Acceptor}\right| - 0.3\right]$$

where E_{HOMO}^{Donor} is for the synthesized polymers, $E_{LUMO}^{Acceptor}$ is for the PCBM, e is the elementary charge, and 0.3 eV is an empirical factor derived from the electron and hole quasi-Fermi energies within the E_{HOMO} and E_{LUMO} energies of the donor and acceptor materials.[79] The computed V_{OC} values for **P1–P5** using this relationship fall between 1.341 V and 1.447 V (Fig. 21 and Table 11). These voltages are higher than the 0.3 V threshold needed to promote effective charge separation and exciton splitting at the donor–acceptor interface, indicating that the synthesized polymers are viable options for organic photovoltaic applications.

4 Conclusion

In summary, the present study focuses on the synthesis of a homopolymer derived from ROMP of dioctyloxy-substituted

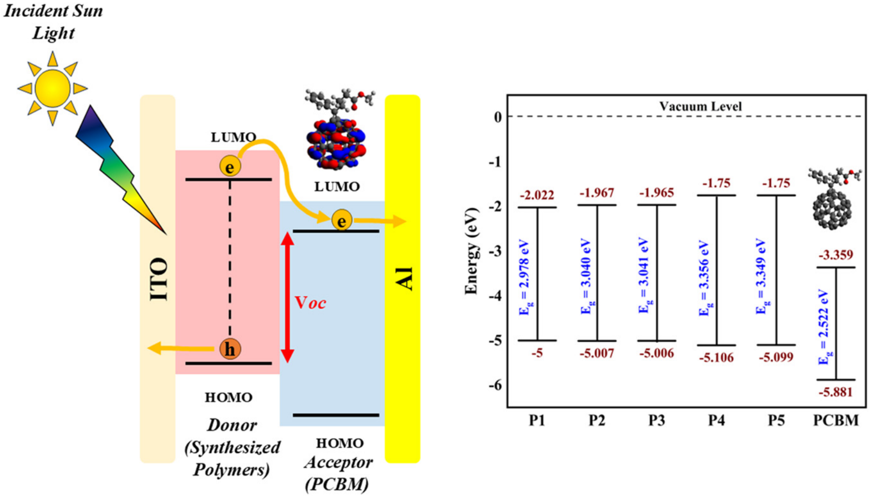

Fig. 21 A visual representation of the V_{OC} and frontier orbital energies of the polymers **P1–P5** and the PCBM.

[2.2]metaparacyclophane-1,9-diene (**DO-*mp*-CPDE**) (**M1**), along with a series of rod–coil copolymers composed of cyclophane-diene (**M1**) and norbornene-based monomers, CH-NDI (**M2**) and AD-NDI (**M3**), with the notable that all synthesized monomers were characterized in ^{1}D and ^{2}D NMR. All polymers were synthesized *via* a living ROMP mechanism, utilizing G2 catalyst in DCE solution.

The kinetic investigation *via* GPC was used to synthesize poly(DO-MPPV) **P1** and copolymers using a block approach in **P2** and **P3**, aiming to gain better control over the polymerization process. Key findings include the lowest PDI for **P1** (1.10) and low PDI values for block copolymers **P2** and **P3** (1.14 and 1.17), indicating uniform molecular weight distributions. The randomly synthesized copolymer **P5** displayed a higher PDI value (1.27), due to high ring strain and unfavorable reaction conditions.

The studied polymers possess remarkable thermal stability, as confirmed by TGA and DSC. TGA analysis revealed that T_d^{onset} ranges from 368.2 °C to 394.6 °C, indicating strong resistance to thermal degradation at elevated temperatures. Furthermore, DSC measurements showed that T_g falls within the range of 108.4 °C to 176.5 °C. SEM analysis of polymer thin films prepared using two protocols revealed different morphologies. The pure THF solution films had a smooth surface due to high solubility. On the other hand, the micellization method showed a different morphology due to the poor solvating ability of methanol. The structural features observed were consistent with UV-Vis absorption results, indicating polymer aggregation.

The optical properties were investigated through three protocols. (a) DCM showed λ_{max} at 408–418 nm and E_g^{op} of 2.53–2.56 eV. (b) Mixing DCM with methanol (micellized state) reduced E_g^{op} to 2.27–2.41 eV, compared to the DCM solution. (c) Thin films had broader absorption, with λ_{max} at 405–425 nm and E_g^{op} ranging from 2.40 to 2.48 eV. Additionally, the electrochemical properties of the polymers were evaluated using CV measurements, which revealed E_g^{elc} values ranging from 2.01 to 2.37 eV, which align with E_g^{op}. Finally, the electronic properties were further studied, and the polymerization patterns were confirmed using the DFT and TD-DFT studies, making them promising for applications in BHJ organic solar cells.

Author contributions

Mohamed E. Abdu: writing – review & editing, writing –original manuscript, visualization, validation, software, resources, project administration, methodology, investigation, formal analysis, data curation, conceptualization. Mohammed F. Radwan: reviewing, editing the original manuscript, and software. Abdulrahman E. Mesbah: writing the DFT section, reviewing, and editing the original manuscript and software. Ye J.hao: software. Abdelrahman Zkria: review & edit, writing – original manuscript. Mahmoud Z. Basyouni: writing, reviewing, and editing the original manuscript and software. Andrew M. Spring: validation, resources, project administration, investigation, supervision, conceptualization.

Conflicts of interest

The authors certify that no known financial or interpersonal conflicts have impacted any of the research provided in this paper.

Data availability

All data generated or analysed during this study are included in this published article and its SI. Supplementary information: chemicals and instruments used, including ^{1}H/^{13}C-NMR, FT-IR, and others, alongside synthesis and characterization procedures for intermediates. To obtain the first monomer, six intermediates were synthesized sequentially: catechol was alkylated to give compound (**1**), which reacted with HBr to yield (**2**); compound (**3**) was prepared by reacting thiourea with benzene. Compounds (**2**) and (**3**) were combined to form seco-urea, which rearranged in the presence of anthranilic acid and isoamyl nitrite to afford compound (**5**), then oxidized with H_2O_2 under air to give intermediate (**6**). Separately, compound (**8**) was obtained *via* a Diels-Alder reaction between cyclopentadiene and maleic anhydride, followed by repeated recrystallization to isolate pure *exo*-norbornene. Polymers **P2–P5** were characterized using ^{1}H-NMR, confirming *cis* and *trans* configurations, and their glass transition temperatures (T_g) were determined by DSC. See DOI: **https://doi.org/10.1039/d5py00818b**.

Acknowledgements

We thank the Hayashi Research Group for their facilities (TGA measurements) and insightful advice. We also extend our gratitude to the LYU GUOWEI Research Group for providing valuable guidance and access to their facilities (DSC measurements).

References

1 C. L. Liu, C. H. Lin, C. C. Kuo, S. T. Lin and W. C. Chen, *Prog. Polym. Sci.*, 2011, **36**, 603–637.
2 M. He, F. Qiu and Z. Lin, *J. Mater. Chem.*, 2011, **21**, 17039–17048.
3 Y. Tao, B. McCulloch, S. Kim and R. A. Segalman, *Soft Matter*, 2009, **5**, 4219–4230.
4 B. D. Olsen and R. A. Segalman, *Mater. Sci. Eng., R*, 2008, **62**, 37–66.
5 A. Meinhard, P. Qi, C. David, I. Maximov and T. F. Keller, *Adv. Mater. Interfaces*, 2024, **2400661**, 1–10.
6 M. Z. Basyouni, M. F. Radwan, M. E. Abdu and A. M. Spring, *Evergreen*, 2024, **11**, 207–213.

7 C. T. Hu, Z. X. Liang, J. Y. Luo, P. H. Chiu, A. I. Day, C. C. Hsieh, P. J. Shih, J. H. Li, B. I. Kuo, I. J. Wang, J. Y. Yen and C. A. Dai, *Biomacromolecules*, 2025, **26**, 4612–4625.

8 C. Höppener, F. H. Sobotta, S. Hoeppener, V. Deckert and J. C. Brendel, *Small*, 2025, **2502157**, 1–11.

9 M. Samandarsangari, R. R. Shulepov, V. A. Baigildin, J. R. Shakirova, V. V. Sokolov, E. V. Durova, D. M. Nikolaev, M. N. Ryazantsev, K. S. Kisel and S. P. Tunik, *Inorg. Chem.*, 2025, **64**, 12742–12754.

10 A. Balafouti and S. Pispas, *Polymers*, 2025, **17**, 1–18.

11 B. Sun, P. Wang, C. Shao, P. Jiang, Y. Guo, S. Yan and W. Fang, *Fuel*, 2025, **385**, 134164.

12 M. E. Abdu, M. F. Radwan, D. A. Elsayed, W. S. Shehab, W. A. Zordok, M. Z. Basyouni and A. M. Spring, *Polymer*, 2025, **333**, 128590.

13 M. Z. Basyouni, M. E. Abdu, M. F. Radwan and A. M. Spring, *J. Mol. Struct.*, 2025, **1338**, 142296.

14 M. F. Radwan, M. E. Abdu, M. M. Elkady, M. Z. Basyouni and A. M. Spring, *Polymer*, 2025, **321**, 128115.

15 H. Lee, D. Kim, J. H. Cho and J. A. Lim, *Acc. Mater. Res.*, 2025, **6**, 434–446.

16 Y. Guo, J. Zhao, L. Chen, H. Zhao, S. Li, Y. Liu, S. Yan and Z. Ren, *Small*, 2025, **2502892**, 1–9.

17 R. Zhang, W. Ning, R. Zhang, Y. Huang and X. Zhang, *Chem. –Eur. J.*, 2025, **31**, e202501480.

18 G. C. Ge, N. Li, Y. J. Hao, L. X. Zhao, X. Wang, L. Liu, X. Chen, H. Liu, Y. Cai and R. S. Zhao, *J. Chromatogr., A*, 2025, **1752**, 465973.

19 C. S. Dziewior, K. Godwin, N. G. Judge, N. Z. Dreger and M. L. Becker, *Prog. Polym. Sci.*, 2024, **156**, 101866.

20 C. H. Chung, Y. C. Huang, S. W. Su, C. J. Su, U. S. Jeng, J. Y. Chen and Y. C. Lin, *Macromol. Rapid Commun.*, 2025, **2401057**, 1–11.

21 M. Z. Basyouni, K. Nomura, Y. Goroumaru, M. F. Radwan, M. E. Abdu and A. M. Spring, *Chem. Pap.*, 2025, **79**, 4687–4700.

22 T. Perumal, C. Krebs de Souza, T. C. Nihues, P. Jain, K. K. Gaikwad and S. Roy, *Food Biosci.*, 2025, **63**, 105656.

23 H. I. Mohamed, M. Z. Basyouni, A. A. Khalil, K. A. Hebash and A. H. Tantawy, *J. Iran. Chem. Soc.*, 2021, **18**, 265–274.

24 R. Stevenson, M. Zhang and G. De Bo, *Polym. Chem.*, 2020, **11**, 2864–2868.

25 Y. Janpatompong, A. M. Spring, V. Komanduri, R. U. Khan and M. L. Turner, *Macromolecules*, 2022, **55**, 10854–10864.

26 F. Liu, P. Qu and M. Weck, *Org. Lett.*, 2022, **24**, 4099–4103.

27 R. Deng, C. Wang and M. Weck, *ACS Macro Lett.*, 2022, **11**, 336–341.

28 Y. Janpatompong, V. Komanduri, R. U. Khan and M. L. Turner, *Org. Biomol. Chem.*, 2023, **21**, 3245–3250.

29 Y. Janpatompong, K. Suwada, M. L. Turner and G. De Bo, *Polym. Chem.*, 2023, **14**, 1978–1982.

30 M. Gwiazda, B. J. Lidster, C. Waters, J. Wongpanich and M. L. Turner, DOI: **10.1021/jacs.4c08985**.

31 A. A. El-Shehawy, M. E. Abdu, M. M. El-Hendawy, M. El-Khouly, M. H. Sherif and H. Y. Moustafa, *J. Phys. Org. Chem.*, 2021, **34**, 1–15.

32 Y. J. Lin, H. Y. Chiang, O. Oki, S. Kushida, S. W. Chang, S. T. Chiu, Y. Yamamoto, T. Hosokai and M. Horie, *ACS Appl. Polym. Mater.*, 2019, **1**, 2240–2248.

33 V. Komanduri, D. R. Kumar, D. J. Tate, R. Marcial-Hernandez, B. J. Lidster and M. L. Turner, *Polym. Chem.*, 2019, **10**, 3497–3502.

34 C. A. Young, A. Hammack, H. J. Lee, H. Jia, T. Yu, M. D. Marquez, A. C. Jamison, B. E. Gnade and T. R. Lee, *ACS Omega*, 2019, **4**, 22332–22344.

35 C. Y. Yu, J. W. Kingsley, D. G. Lidzey and M. L. Turner, *Macromol. Rapid Commun.*, 2009, **30**, 1889–1892.

36 T. Wu, Y. Liu, J. Ye, Y. Chen, G. Dai, X. Zhang and Y. Zhao, *J. Power Sources*, 2024, **612**, 234779.

37 M. Carratù, R. Troiano, C. Costabile, A. C. Boccia, S. Pragliola and F. Grisi, *Eur. Polym. J.*, 2023, **200**, 112539.

38 J. Asrar, *Macromolecules*, 1992, **25**, 5150–5156.

39 K. H. Yoon, K. O. Kim, M. Schaefer and D. Y. Yoon, *Polymer*, 2012, **53**, 2290–2297.

40 F. Yu, A. M. Spring, L. Li, F. Qiu, K. Yamamoto, D. Maeda, M. Ozawa, K. Odoi and S. Yokoyama, *J. Polym. Sci., Part A: Polym. Chem.*, 2013, **51**, 1278–1284.

41 A. M. Spring, F. Yu, F. Qiu, K. Yamamoto and S. Yokoyama, *Polym. J.*, 2014, **46**, 576–583.

42 A. M. Spring, D. Maeda, M. Ozawa, K. Odoi, F. Qiu, K. Yamamoto and S. Yokoyama, *Polym. Bull.*, 2015, **72**, 503–521.

43 A. M. Spring, F. Qiu and S. Yokoyama, *Eur. Polym. J.*, 2016, **84**, 89–99.

44 A. Mandal, I. Mandal and A. F. M. Kilbinger, *ACS Macro Lett.*, 2022, **11**, 491–497.

45 D. A. Elsayed, M. E. Abdu, M. A. Marzouk, E. M. Mahmoud, W. H. El-Shwiniy, A. M. Spring and W. S. Shehab, *Sci. Rep.*, 2024, **14**, 1–19.

46 C. Y. Yu, M. Horie, A. M. Spring, K. Tremei and M. L. Turner, *Macromolecules*, 2010, **43**, 222–232.

47 B. Ö. Öztürk, E. Yakut, E. Ak and S. K. Şehitoğlu, *React. Funct. Polym.*, 2017, **111**, 22–29.

48 A. M. Spring, F. Qiu, J. Hong, A. Bannaron, T. Kashino, T. Kikuchi, M. Ozawa, H. Nawata, K. Odoi and S. Yokoyama, *Eur. Polym. J.*, 2017, **97**, 263–271.

49 C. J. Lin, Y. H. Lin, T. C. Chiang and C. Y. Yu, *Polymer*, 2022, **260**, 125374.

50 S. Hou, Durham theses, Durham University, 2016.

51 T. W. Hsu, S. J. Kempel and Q. Michaudel, *J. Polym. Sci.*, 2022, **60**, 569–578.

52 F. Menk, M. Mondeshki, D. Dudenko, S. Shin, D. Schollmeyer, O. Ceyhun, T. L. Choi and R. Zentel, *Macromolecules*, 2015, **48**, 7435–7445.

53 S. Sutthasupa, M. Shiotsuki and F. Sanda, *Polym. J.*, 2010, **42**, 905–915.

54 A. A. El-Shehawy, N. I. Abdo, A. A. El-Barbary and J. S. Lee, *Eur. J. Org. Chem.*, 2011, 4841–4852.

55 A. M. Wallace, C. Curiac, J. H. Delcamp and R. C. Fortenberry, *J. Quant. Spectrosc. Radiat. Transfer*, 2021, **265**, 107544.

56 A. A. El-Shehawy, N. I. Abdo, M. M. El-Hendawy, A. R. I. A. Abdallah and J. S. Lee, *J. Phys. Org. Chem.*, 2020, **33**, 1–17.

57 R. Li, Y. Mo, R. Shi, P. Li, C. Li, Z. Wang, X. Wang and S. Li, *Monatsh. Chem.*, 2014, **145**, 85–90.

58 R. López, *Adv. Math.*, 2014, **262**, 476–483.

59 F. Neese, *J. Comput. Chem.*, 2023, **44**, 381–396.

60 S. Ghomrasni, S. Ayachi and K. Alimi, *J. Phys. Chem. Solids*, 2015, **76**, 105–111.

61 F. Neese, *J. Comput. Chem.*, 2003, **24**, 1740–1747.

62 F. Neese, F. Wennmohs, A. Hansen and U. Becker, *Chem. Phys.*, 2009, **356**, 98–109.

63 B. Helmich-Paris, B. de Souza, F. Neese and R. Izsák, *J. Chem. Phys.*, 2021, **155**, 104109.

64 A. D. Becke, *J. Chem. Phys.*, 1993, **98**, 5648–5652.

65 V. B. Kumar, S. Śmiga and I. Grabowski, *J. Phys. Chem. Lett.*, 2024, **15**, 10219–10229.

66 F. Sousa, P. A. Fernandes and M. J. Ramos, *J. Phys. Chem. A*, 2007, **111**, 10439–10452.

67 S. Mahmoudi, M. M. Dehkordi and M. H. Asgarshamsi, *J. Mol. Model.*, 2021, **27**, 271.

68 W. S. Shehab, H. A. Haikal, D. A. Elsayed, A. F. El-Farargy, A. R. B. A. El-Gazzar, G. T. El-Bassyouni and S. M. Mousa, *Sci. Rep.*, 2024, **14**, 1–14.

69 T. Yanai, D. P. Tew and N. C. Handy, *Chem. Phys. Lett.*, 2004, **393**, 51–57.

70 W. S. Shehab, N. Magdy, M. A. R. Elhoseni, M. G. Assy, M. H. M. AbdEl-Azim, A. E. Mesbah, W. H. El-Shwiniy, M. M. K. Amer and D. A. Elsayed, *J. Mol. Struct.*, 2025, **1337**, 142163.

71 M. M. Jadhav, J. V. Vaghasiya, D. Patil, S. S. Soni and N. Sekar, *J. Photochem. Photobiol., A*, 2019, **377**, 119–129.

72 S. Ennehary, H. Toufik, S. M. Bouzzine and F. Lamchouri, *J. Comput. Electron.*, 2020, **19**, 840–848.

73 J. Sworakowski, *Synth. Met.*, 2018, **235**, 125–130.

74 K. Sohlberg and M. E. Foster, *RSC Adv.*, 2020, **10**, 36887–36896.

75 A. M. Spring, F. Qiu, J. Hong, A. Bannaron, X. Cheng and S. Yokoyama, *Polymer*, 2019, **172**, 382–390.

76 H. Meier, U. Stalmach and H. Kolshorn, *Acta Polym.*, 1997, **48**, 379–384.

77 H. A. M. Van Mullekom, J. A. J. M. Vekemans, E. E. Havinga and E. W. Meijer, in *Developments in the chemistry and band gap engineering of donor-acceptor substituted conjugated polymers*, 2001, vol. 32.

78 J. Rissler, *Chem. Phys. Lett.*, 2004, **395**, 92–96.

79 F. C. Franco and A. A. B. Padama, *Polymer*, 2016, **97**, 55–62.